RESEARCH ARTICLE

WILEY

Neural sensitivity to translational self- and object-motion velocities

Valentina Sulpizio[1,2] ⓘ | **Alessandro von Gal**[2] | **Gaspare Galati**[1,2] ⓘ | **Patrizia Fattori**[3] | **Claudio Galletti**[3] | **Sabrina Pitzalis**[1,4] ⓘ

[1]Department of Cognitive and Motor Rehabilitation and Neuroimaging, Santa Lucia Foundation (IRCCS Fondazione Santa Lucia), Rome, Italy

[2]Department of Psychology, Sapienza University, Rome, Italy

[3]Department of Biomedical and Neuromotor Sciences, University of Bologna, Bologna, Italy

[4]Department of Movement, Human and Health Sciences, University of Rome "Foro Italico", Rome, Italy

Correspondence
Valentina Sulpizio, IRCCS Santa Lucia Foundation, Via Ardeatina, 306, 00179 Rome, Italy.
Email: v.sulpizio@hsantalucia.it

Abstract

The ability to detect and assess world-relative object-motion is a critical computation performed by the visual system. This computation, however, is greatly complicated by the observer's movements, which generate a global pattern of motion on the observer's retina. How the visual system implements this computation is poorly understood. Since we are potentially able to detect a moving object if its motion differs in velocity (or direction) from the expected optic flow generated by our own motion, here we manipulated the relative motion velocity between the observer and the object within a stationary scene as a strategy to test how the brain accomplishes object-motion detection. Specifically, we tested the neural sensitivity of brain regions that are known to respond to egomotion-compatible visual motion (i.e., egomotion areas: cingulate sulcus visual area, posterior cingulate sulcus area, posterior insular cortex [PIC], V6+, V3A, IPSmot/VIP, and MT+) to a combination of different velocities of visually induced translational self- and object-motion within a virtual scene while participants were instructed to detect object-motion. To this aim, we combined individual surface-based brain mapping, task-evoked activity by functional magnetic resonance imaging, and parametric and representational similarity analyses. We found that all the egomotion regions (except area PIC) responded to all the possible combinations of self- and object-motion and were modulated by the self-motion velocity. Interestingly, we found that, among all the egomotion areas, only MT+, V6+, and V3A were further modulated by object-motion velocities, hence reflecting their possible role in discriminating between distinct velocities of self- and object-motion. We suggest that these egomotion regions may be involved in the complex computation required for detecting scene-relative object-motion during self-motion.

KEYWORDS
brain mapping, flow parsing, functional magnetic imaging, motion detection, optic flow, virtual reality

1 | INTRODUCTION

Everyday interactions with the environment require a correct estimation of both self- and object- motion velocities. Self-motion perception has a key role in the guidance of our actions toward objects and in navigation, through the updating of the spatial relationship between one's position and the position of the surrounding objects. Perception of object-motion speed is essential to approach or avoid them properly. In many circumstances, object-motion perception is complicated by concomitant self-motion, generating a global pattern of motion (optic flow) on the observer's retina (Gibson, 1950). One of the main challenges for the visual system is to determine the source of the movement that generates the flow pattern: self-motion, object-motion, or their combination.

The neural representation of self-motion perception has been extensively studied in both macaques and humans. In monkeys, an optic flow stimulation that is compatible with self-motion is able to activate a series of higher-level motion areas, such as the ventral intraparietal area (VIP; Bremmer et al., 2001; Duhamel et al., 1998), the middle superior temporal area (MST; Duffy, 1998), and the caudal portion of the posterior parietal cortex (PEc; Raffi et al., 2002). In addition, we recently revealed in a fMRI study on macaque monkeys (Pitzalis et al., 2021) that also the medial motion area V6 (Galletti et al., 1996, 1999) is responsive to flow fields. In humans, recent human neuroimaging studies revealed the existence of a wider network of higher-level multisensory cortical regions (called egomotion regions) that are sensitive to optic processing, that is, the V6 complex (or V6+, involving the two retinotopic regions V6 and V6Av; Pitzalis et al., 2006, 2010; Pitzalis, Fattori, et al., 2013; Tosoni et al., 2015; Serra et al., 2019; see also Sulpizio et al., 2023 for a recent review) in the parietal occipital sulcus, the MT complex (or MT+; Morrone et al., 2000; Pitzalis, Bozzacchi, et al., 2013; Sulpizio et al., 2022; Tootell et al., 1995) in the lateral temporo-occipital cortex, area V3A (Orban et al., 2003; Pitzalis et al., 2010; Serra et al., 2019; Sulpizio et al., 2020; Sunaert et al., 1999; Tootell et al., 1997) in the transverse occipital sulcus, the putative human homolog of area VIP in the intraparietal sulcus (IPSmot; Bremmer et al., 2001, Cardin & Smith, 2010, Pitzalis, Sdoia, et al., 2013, Sereno & Huang, 2006), the cingulate sulcus areas (CSv and pCi; Serra et al., 2019; Wall & Smith, 2008), the adjacent precuneus (PEc; Pitzalis et al., 2019), and the posterior insular cortex (PIC; Frank et al., 2014).

The neural representation of object-motion perception has been studied especially in the monkey brain. Studies focusing on individual units have revealed the presence of "real motion" cells in various cortical regions within the visual stream, including V1 (Bridgeman, 1973; Galletti et al., 1984), V2 (Galletti et al., 1988), V3A (Galletti et al., 1990), V6 (Galletti & Fattori, 2003), MT/V5 (Erickson & Their, 1991), MST (Erickson & Their, 1991), and 7a (Sakata et al., 1985). All these areas respond to real movements of an object in the visual field, but much less or not at all to the retinally equivalent movement of its image as induced, for instance, by eye movements. Additionally, macaque area MT has been observed to contribute to the detection of object-motion during self-motion by selectively responding to local conflicts between disparity and motion parallax cues (Kim et al., 2016; Kim et al., 2022; Nadler et al., 2013). In humans, object-motion perception has received comparatively less attention. Some recent studies demonstrated a critical role of areas V3A and V6 in detecting the "real" movement of an object in the visual field, being these areas able to compensate for self-induced visual motion during both eye movements (Fischer et al., 2012; Nau et al., 2018) and voluntary head movements (Schindler & Bartels, 2018a, 2018b). Additionally, neuroimaging evidence during natural vision revealed that perception of object-motion involves motion-selective regions such as MT+ and the lateral occipital cortex (Bartels et al., 2008). Similarly, Calabro and Vaina (2012) demonstrated that a network of interacting occipital (V3A, KO, and MT+) and parietal (VIP, dorsal IPS medial or DIPSM; Orban et al., 2003) areas provides the neuronal substrate for object-motion processing.

From an ecological point of view, one of the most ubiquitous scenarios in perception of visual motion includes a combination of self- and object-motion. For example, when an observer moves through the environment, the capacity to detect and assess world-relative object-motion is critical for safe and successful interaction with the environment. However, this could be a difficult task for the brain since it requires to segregate the image motion generated on the retina into self- and object-motion components. Human behavioral studies suggest that the brain may use its sensitivity to self-motion compatible optic flow (likely supported by egomotion regions -see above-) to estimate and subtract self-motion from the overall retinal motion to isolate object-motion: this mechanism has been named "flow parsing" (see Rushton & Warren, 2005; Warren & Rushton, 2009). How the human brain might achieve this computation remains largely unknown.

A way to test how the brain accomplishes the flow parsing computation is to manipulate the relative motion velocity between the observer (the self) and the object within a stationary scene. In line of principle, one could detect a moving object if its motion differs in velocity (or direction) from the expected optic flow generated by the observer's motion. In the present study, we tested the neural sensitivity of egomotion regions (CSv, pCi, PIC, V6+, V3A, IPSmot/VIP, and MT+) to a combination of different velocities of visually induced translational self- and object-motion within a virtual scene while participants were instructed to detect object-motion. This allowed us to test the brain sensitivity to both pure (self-motion only or object-motion only) and double-source (combined self- and object-motion) motion conditions as well as towards different motion (both self- and object-based) velocities. To this aim, we used a combined approach of individual surface-based brain mapping, task-evoked activity by fMRI, and advanced procedures of data analysis (parametric and representational similarity analyses) to examine how the cortical nodes specialized in motion perception contribute to differentiate between distinct velocities of self- and object-motion, unveiling the potential neural signature of the complex computation required for detecting scene-relative object-motion during self-motion.

2 | METHODS

2.1 | Participants

Twenty-six neurologically normal volunteers (nine females, mean age 24 s.d. 2.6) participated in the study. The sample size of this study was determined based on a previous study (Pitzalis et al., 2020). We first calculated the effect size of the previous study (Cohen's $d = .899$), and then estimated the required sample size using G*Power (Version 3.1.9.7; Faul et al., 2007) with default parameters ($\alpha = 0.05$, $1 - \beta = .95$), which resulted in a sample size of $n = 16$. A further sensitivity analysis was conducted to calculate the minimal effect across various sample sizes around $n = 20$ (Table S1). The minimal effect size for $n = 26$ is 0.66. All participants were right-handed based on the Edinburgh Handedness Inventory (Oldfield, 1971) and had either normal or corrected-to-normal vision. Written informed consent was obtained from all volunteers participating in this study, which received approval from the local research ethics committee of the IRCCS Fondazione Santa Lucia in Rome, following the principles of the Declaration of Helsinki.

2.2 | The main "bus experiment"

In the main event-related fMRI experiment, hereafter called "bus experiment," participants were presented with a series of movies and snapshots taken from a realistic virtual environment reproducing different combinations of visually induced self- and object-motion. This realistic motion stimulation was obtained by using the virtual reality software Unity (version 2018 3.11f1; https://unity.com).

The virtual reality environment (Figure 1a) contained three major elements:

1. The background: a field of green grass with a road, and a series of randomly placed 3D trees (positioned on the other side of the road with respect to the field and at a distance between 25 and 65 m from the observer). The high density of trees was chosen to induce a strong vection, that is, the compelling illusion of self-motion produced by a purely visual stimulation.

2. The virtual camera: the point of view of the observer (self). The camera, which was located 20 virtual meter away from the road,
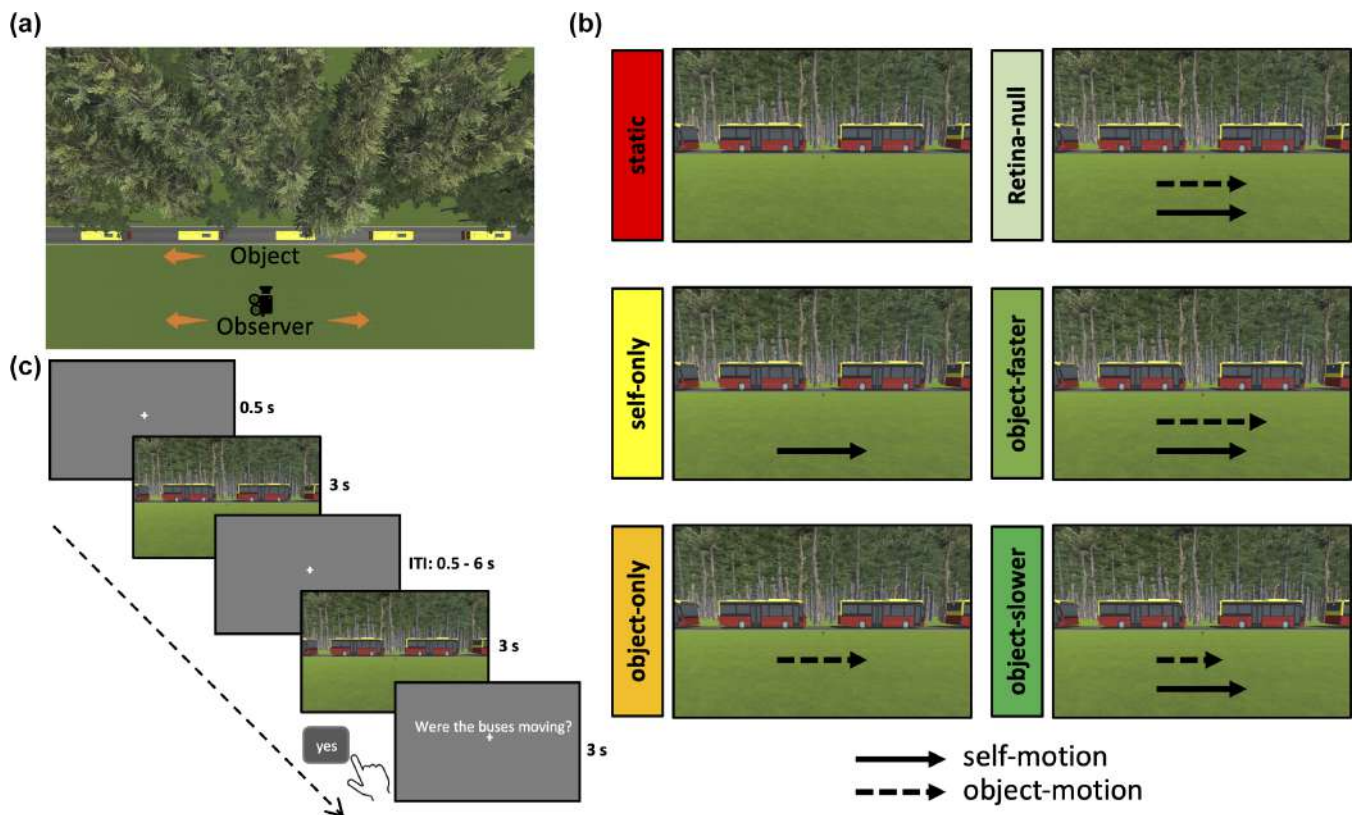

FIGURE 1 Virtual reality environment and schematic representations of stimulus conditions. (a) A 2D visual representation of virtual environment from a top perspective is shown. (b) Static frames and still frames from the 3-s movies reproducing the five motion conditions (self-only, object-only, retinal-null, object-faster, and object-slower) are shown. Color codes are used here for illustrative purpose only and correspond to the ones used in Figure 2b. The solid black arrow indicates the simulated observer's motion direction. The dashed black arrow indicates the object (the row of buses) motion direction. The length of the arrows indicates the amount of motion velocity. All the examples show rightward motion. Both leftward and rightward translational motions were presented although in separate runs. (c) Example of trial sequence and timeline. Participants were presented with a series of movies reproducing different combinations of self- and object-motion and they were instructed to answer the question trial referring to the immediately preceding trial.

always translated sideways (leftward or rightward) along a path that was parallel to the road (see arrows in Figure 1a, bottom).

3. The buses (object): a row of 25 red buses placed on the road, 25 virtual meter away from the observer. The use of more than one bus was justified by the need to make sure that the buses were always present in the observer's visual field. All the buses could translate sideways (leftward or rightward) but always coherently with the camera direction, thus following the same direction as the observer's motion (see arrows at the center of Figure 1a). This situation is typically observed when we are looking out from the lateral window of a car in motion while another car is moving in the same direction.

Both the observer and the object traveled at constant speed with zero acceleration (uniform rectilinear motion). To explore the neural sensitivity for different motion velocities, we manipulated the amount of self- and object-motion velocity so that we obtained six experimental conditions (see Figure 1b). Each condition has been consistently associated for clarity to a specific color in all figures in the article as follows:

- Static (red): both the observer and the object were completely still on the scene.
- Self-only (yellow): the observer was moving while the object remained still on the scene. The simulated self-motion velocity could be 20, 40, 60, or 80 km/h. This visual stimulation was consistent with pure self-motion within a static environment.
- Object-only (orange): the buses were moving while the observer remained still on the scene. The simulated object-motion velocity could be 20, 40, 60, or 80 km/h (corresponding to the angular velocity on the participant's retina of 9.5, 18.9, 28.4, 37.9, and 47.4 deg/s, respectively). This visual stimulation was consistent with pure object-motion within a static environment.
- Retinal-null (light green): the observer and the object moved at the same velocity (and direction). As a result, the object appeared still on the retina. The self- and object-motion velocities could be 20, 40, 60, or 80 km/h.
- Object-faster (medium green): the object moved 20 km/h faster than the observer, whose velocity could be 20, 40, 60, or 80 km/h as above.
- Object-slower (dark green): the object moved 20 km/h slower than the observer, whose velocity could be 40, 60, 80, or 100 km/h.

The static condition was introduced as a high-level control condition. Self- and object-only conditions were introduced to selectively test the neural sensitivity to pure self- and object-motion stimulations, respectively. The double-source motion conditions (i.e., retinal-null, object-slower, and object-faster) were introduced to test the neural sensitivity toward complex motion stimulation combining self- and object-motion. In particular, the retinal-null condition was used to test the neural sensitivity toward the world-centered motion of an object in the absence of its retinal motion. This is typically observed when the observer moves at the same velocity (and direction) of the object.

The two latter conditions (object-faster and object-slower) gave us the opportunity to test the sensitivity to different object (and self) velocities, keeping the amount of object retinal motion constant. To this aim, object- and self-motion velocities were set so that the retinal motion velocity (the difference between the two) was always 20 km/h.

Figure 1c shows a typical trial sequence. Each trial consisted in the observation of a 3-s movie/snapshot belonging to either of the above-described experimental conditions. During each scan, a different pseudorandomized (counterbalanced) sequence (i.e., trial order was different for each scan but fixed across subjects) was presented. This sequence included a total of 77 trials: 12 different trials for each of the six conditions, plus 5 question trials (see below). The distribution of inter-trial intervals (ITIs: the time between the end of a trial and the beginning of the next one) was defined as a truncated exponential distribution (see Neurodesign: https://github.com/neuropower/neurodesign) between a minimum ITI of 0.5 s and a maximum ITI of 6 s, with a mean ITI of 2 s and a median ITI of 1.4 s. During the ITI periods, a white central cross was presented on a dark green background. The dark green color (corresponding to the mean color extracted by the experimental trials) was used to minimize the brisk on–off switch induced by changes in brightness between consecutive stimuli.

Participants were required to keep central fixation, and eye tracking was performed online during the main experiment. This ensures that the velocity of the object-motion on the retina (which is derived by subtracting the self from the object-motion velocity) is not confounded by the retinal shifts generated by eye movements. To this aim, an infrared eye-tracking system (60 Hz video-based with long-range optics, LiveTrack AV for fMRI—Presto—) was used to monitor gaze stability throughout the experiment. After blink removal, drifts due to changes in head position were removed. Fixation accuracy was quantified by calculating the root-mean-square error (RMSE) of the actual eye position relative to the eye position during fixation only for each stimulus condition separately, across sessions and subjects ($n = 139$). Seventeen runs were excluded due to technical problems (i.e., loss of trace) in data collection. RMSE values were submitted to two separate one-way ANOVAs with condition (static, self-only, object-only, retinal-null, object-faster, and object-slower) as factor. The ANOVAs revealed no main effect of condition for both X ($F_{5, 690} = 2.04$; $p = .07$; $\eta p2 = 0.01$) and Y ($F_{5, 690} = 1.05$; $p = .38$; $\eta p2 = 0.008$) coordinates of the eye position. Table S2 shows mean values (±SE) of RMSE for each experimental condition.

Participants were also required to continuously check for the presence of object-motion because, in some circumstances (10% of the total trials, i.e., questions trials), they would be explicitly asked to answer to the question "Were the buses moving?" which referred to the immediately preceding trial (see Figure 1c). Participants were instructed that the questions trials might appear randomly and they were required to respond using the fMRI-compatible keypad. Specifically, they were instructed to press the "yes" button with their right index finger if the target object (the row of buses) was in motion, or to press the "no" button with their middle finger if there was no

object-motion. These questions were introduced to ensure that participants were keeping attention to the task. Behavioral responses were recorded during each scan. We then calculated for each participant the percentage of correct responses averaged across scans. The percentage of correct responses averaged across subjects was equal to 97% (SD = 0.03), indicating a good ability of the participant to detect object-motion.

2.3 | Functional localizer

To identify egomotion-responsive areas CSv, pCi, PIC, V6+, V3A, IPS-mot/VIP, and MT+ (Figure 2a), a separate localizer paradigm was used (Serra et al., 2019; Sulpizio et al., 2020). The stimulus (the flow fields; see Pitzalis et al., 2010 for a more detailed description) consisted of coherently moving fields of dots simulating the visual stimulation typically observed during self-motion. While keeping central fixation, participants were presented with four blocks of coherently moving dot fields interleaved with four blocks of randomly moving dot fields, each lasting 16 s. Every 0.5 s, a new field of white dots was generated. During blocks of coherent motion, the new field of white dots randomly showed a different motion pattern ranging from spirals, dilations, rotations, and contractions. The center of the movement was jittered from flow to flow, and the dot speed was logarithmically scaled with eccentricity (average speed: 25°/s; range of speed variance: 17°/s–33°/s).

2.4 | Image acquisition

MR images were acquired at the Santa Lucia Foundation (Rome, Italy) on a 3 T Siemens MAGNETOM Prisma MR scanner using a 64-channel head coil. Functional T2*-weighted images were collected using a multiband gradient echo EPI sequence using blood-oxygenation level-dependent imaging (Kwong et al., 1992). The following parameters were used: repetition time (TR) = 0.8 s, echo time (TE) = 0.03 s, 88 × 88 image matrix, flip angle = 52°, 60 slices, AC-PC plane orientation, interleaved excitation order, in-plane pixel size = 2.4 mm, slice thickness = 2.4 mm, and multiband factor = 6.

Structural images were collected using a sagittal magnetization-prepared rapid acquisition gradient echo (MPRAGE) T1-weighted sequence (TR = 2.5 s, TE = 0.002 s, inversion time [TI] = 1.08 s, flip angle = 8°, 256 × 256 mage matrix, in-plane pixel size = 1 mm, and 176 contiguous slices).

Two spin-echo EPI volumes with phase encoding in opposite directions, no multiband acceleration, and the same geometrical and sampling properties of functional runs were acquired for field mapping (TE = 80 ms, TR = 7000 ms). A single-band reference (SBRef) image associated with the BOLD series was acquired at the beginning of each data run as the reference image.

In each scan, the first four volumes were discarded from data analysis, and the experimental tasks started at the beginning of the fifth volume. The number of volumes per acquisition scan was 484 for

the main experiment and 324 for the localizer. Each participant underwent six consecutive fMRI acquisition scans (three for leftward translations and three for right translations) for the main experiment. Each of these scans, which contained all the above-described experimental conditions in a balanced manner, lasted approximately 7 min. The order of these scans was counterbalanced across participants. Participants also underwent a localizer scan lasting approximately 4 min.

2.5 | Image preprocessing

Results included in this manuscript come from preprocessing performed using *fMRIPrep* 20.2.6 (Esteban et al., 2018; RRID:SCR_016216), which is based on *Nipype* 1.7.0 (Gorgolewski et al., 2011; RRID:SCR_002502). The description below is an excerpt from the text automatically generated by fMRIPrep with the express intention to be copied and pasted into manuscripts. It is released under the CC0 license.

2.5.1 | Anatomical data preprocessing

The T1-weighted (T1w) image was corrected for intensity non-uniformity (INU) with N4BiasFieldCorrection (Tustison et al., 2010), distributed with ANTs 2.3.3 (RRID:SCR_004757), and used as T1w-reference throughout the workflow. The T1w-reference was then skull-stripped with a *Nipype* implementation of the antsBrainExtraction.sh workflow (from ANTs), using OASIS30ANTs as target template. Brain tissue segmentation of cerebrospinal fluid (CSF), white-matter (WM), and gray-matter (GM) was performed on the brain-extracted T1w using fast (FSL 5.0.9, RRID:SCR_002823, Zhang et al., 2001). Brain surfaces were reconstructed using recon-all (FreeSurfer 6.0.1; RRID:SCR_001847; Dale et al., 1999), and the brain mask estimated previously was refined with a custom variation of the method to reconcile ANTs-derived and FreeSurfer-derived segmentations of the cortical gray-matter of Mindboggle (RRID:SCR_002438; Klein et al., 2017).

2.5.2 | Functional data preprocessing

For each of the BOLD scans acquired per subject (across all tasks), the following preprocessing was performed. First, a reference volume and its skull-stripped version were generated by the single-band reference (SBRef). The *fieldmap* was then co-registered to the target EPI reference scan and converted to a displacement field map (amenable to registration tools such as ANTs) with FSL's fugue and other *SDCflows* tools. Based on the estimated susceptibility distortion, a corrected EPI (echo-planar imaging) reference was calculated for a more accurate co-registration with the anatomical reference. The BOLD reference was then co-registered to the T1w reference using bbregister (FreeSurfer) which implements boundary-based registration (Greve & Fischl, 2009). Co-registration was configured with 12 degrees of

freedom to account for distortions remaining in the BOLD reference. Head-motion parameters with respect to the BOLD reference (transformation matrices, and six corresponding rotation and translation parameters) were estimated before any spatiotemporal filtering using mcflirt (FSL 5.0.9; Jenkinson et al., 2002). BOLD scans were slice-time corrected to 0.351 s (half of slice acquisition time) using 3dTshift from AFNI 20160207 (Cox & Hyde, 1997; RRID:SCR_005927).

The BOLD time series (including slice-timing correction) was resampled with a single interpolation step by composing all the pertinent transformations (i.e., head-motion transform matrices, susceptibility distortion correction, and co-registrations to anatomical and output spaces) onto the *fsaverage* FreeSurfer surface using mri_vol2-surf (FreeSurfer). A final *grayordinates* file (Glasser et al., 2013) containing 91k samples was generated using the highest-resolution fsaverage as intermediate standardized surface space. Finally, we used wb_command (Connectome Workbench) to extract the surface-based portions of grayordinates file in the standard fsLR-32k space (Glasser et al., 2013) and to smooth them using a surface-based Gaussian smoothing with a 4-mm full-width at half-maximum (FWHM) kernel.

For each time series, framewise displacement (FD) was computed using the implementations in *Nipype* (following the definitions by Power et al., 2014). These values were obtained from the realignment parameters estimated during the preprocessing phase and indicated the amount (in mm) of head movement relative to the previous time point. FD values were included as nuisance regressors in all the BOLD analyses to reduce motion-induced artifacts.

2.6 | Image analyses

We analyzed functional images for each participant separately on a vertex-by-vertex basis, according to the general linear model as implemented in SPM12 (http://www.fil.ion.ucl.ac.uk/spm).

The analyses were conducted on a set of regions of interest (ROIs) that are independently defined and theoretically motivated. We identified these regions, that is, the egomotion regions by analyzing data from the "localizer" scan. Specifically, we modeled "active" blocks of coherent moving dots as box-car functions convolved with a canonical hemodynamic response function and used them as predictors in a general linear model (GLM). We did not explicitly modeled blocks of random motion as GLM regressors, treating them as part of residual variance.

Seven egomotion regions (see Figure 2a) were identified by comparing coherently versus randomly moving dots: (1) the cingulate sulcus visual area (CSv), likely corresponding to the motion area originally described by Wall and Smith (2008), located in the posterior part of the cingulate sulcus (2) the posterior cingulate sulcus area (pCi), likely corresponding to area Pc (as Precuneus) identified by Cardin and Smith (2010), located in posterior dorsal tip of the cingulate sulcus; (3) the posterior insular cortex (PIC), in correspondence of the junction between the posterior parietal cortex and the posterior insula (see Greenlee et al., 2016 for a review); (4) the V6 complex (or V6+) located in the dorsalmost part of the parieto-occipital sulcus (POS), which includes the retinotopic areas V6 (Pitzalis et al., 2010) and,

anteriorly, V6Av (Pitzalis, Sereno, et al., 2013; Tosoni et al., 2015); (5) the caudalmost portion of the posterior intraparietal sulcus (pIPS), well in correspondence with the dorsal portion of the retinotopically defined V3A (Pitzalis et al., 2010; Sereno et al., 2001; Tootell et al., 1997); (6) the motion area identified in the horizontal segment of the IPS (IPSmot), likely corresponding to the human homologue of VIP (see Huang & Sereno, 2018 for a review); (7) the lateral occipito-temporal MT complex (MT+; Cardin & Smith, 2010; Serra et al., 2019), in correspondence of the retinotopic cluster MT+ identified by Kolster et co-workers (2010).

All these egomotion regions were defined on the cortical surface reconstruction of each individual hemisphere and created by using a data-driven and threshold-free mapping. Specifically, single activation peaks and their neighborhood (for a maximum of 400 cortical nodes) were selected using a watershed segmentation algorithm applied to surface meshes (Mangan & Whitaker, 1999). This procedure enables the segmentation of activation maps into separate "neighborhoods." It starts from all activation peaks (i.e., local maxima) in the map and follows the descending gradient of activation in all directions around each peak until the whole cluster is "filled." All these ROIs were successfully identified in all participants, except for area MT+ that was identified in 50/52 hemispheres. Table 1 reports MNI coordinates of the peaks of all individually defined regions, averaged across subjects, the extent (number of nodes), and the mean peak *t* value for each region.

We then interrogated these ROIs with respect to the main experiment (bus experiment). For what concerns the analyses of the bus experiment, each trial was modeled as a canonical hemodynamic response function time-locked to the trial onset. For each trial type (static, self-only, object-only, retinal-null, object-faster, and object-slower), separate regressors were included across motion direction (leftward or rightward), so that parameter estimates for the average hemodynamic response evoked by each trial type was obtained. Fixation blocks were not explicitly modeled as GLM regressors; they were treated as part of the residual variance. As a control, in a separate analysis, we also modeled the two motion directions (leftward and rightward).

For each participant, we estimated the amplitude of the hemodynamic response in each ROI. This estimate was obtained by using a weighted spatial average across all vertices within each ROI of the surface-transformed unsmoothed BOLD time series. We first analyzed these regional hemodynamic responses by means of a series of one-sample *t* tests against zero to assess the presence of a reliable activation in each condition. This procedure was crucial to determine the motion condition to which the region was sensitive. A Bonferroni correction ($p = .05/N =$ number of conditions) was applied to account for multiple comparisons. As a second step, the regional hemodynamic responses, which are shown in the plots in Figure 2b, were analyzed separately for each region through a series of one-way ANOVAs with condition (static, self-only, object-only, retinal-null, object-faster, and object-slower) as factor. For these analyses, post hoc comparisons were computed after finding significant main effects, as paired *t* tests between all the pairwise comparisons between the factor levels, using Bonferroni adjustment to correct for multiple

TABLE 1 MNI coordinates (mm) of ROIs.

Region	Hemisphere	MNI coordinates			Number of nodes	Peak T-value	Size (mm²)
		X	Y	Z			
CSv	LH	−13 ± 2	−24 ± 6	42 ± 4	265 ± 89	5.02 ± 2	485 ± 186
	RH	12 ± 3	−24 ± 7	44 ± 5	252 ± 101	4.89 ± 2	403 ± 167
MT+	LH	−43 ± 4	−71 ± 7	1 ± 5	170 ± 111	5.20 ± 2	265 ± 169
	RH	46 ± 4	−62 ± 4	1 ± 4	129 ± 72	4.76 ± 2	231 ± 149
pCi	LH	−14 ± 2	−45 ± 4	56 ± 5	196 ± 97	4.18 ± 2	297 ± 163
	RH	12 ± 3	−43 ± 4	59 ± 5	264 ± 102	4.83 ± 2	446 ± 172
PIC	LH	−48 ± 6	−37 ± 5	24 ± 5	312 ± 119	7.44 ± 2	560 ± 217
	RH	53 ± 9	−32 ± 3	22 ± 5	330 ± 96	6.00 ± 2	516 ± 153
V3A	LH	−21 ± 3	−79 ± 6	35 ± 9	220 ± 89	7.35 ± 3	507 ± 197
	RH	26 ± 4	−76 ± 7	36 ± 8	227 ± 96	7.03 ± 3	537 ± 203
V6+	LH	−15 ± 3	−81 ± 5	35 ± 7	215 ± 87	8.82 ± 3	528 ± 229
	RH	18 ± 3	−78 ± 4	35 ± 7	215 ± 87	8.70 ± 3	565 ± 248
IPSmot/VIP	LH	−27 ± 5	−57 ± 6	57 ± 6	197 ± 98	5.57 ± 3	276 ± 141
	RH	29 ± 4	−56 ± 6	52 ± 5	211 ± 120	5.15 ± 2	264 ± 161

Note: Mean values (±standard deviation) of peaks of individually defined regions, size as the number of nodes and area (mm²), and the statistical significance as peak *t* values are reported.

Abbreviations: CSv, cingulate sulcus visual area; LH, left hemisphere; pCi, posterior cingulate sulcus area; PIC, posterior insular cortex; RH, right hemisphere; ROI, region of interest; VIP, ventral intraparietal area.

comparisons. Finally, paired *t* tests were used to assess any difference between the two motion directions (leftward and rightward).

Beyond the regional approach, a whole-brain analysis was conducted to have a general picture of brain regions involved in different combinations of self- and object-motion. A series of "omnibus" F-contrasts (thresholded at *p* < .01, corrected for multiple comparisons based on family-wise error (FWE), with a cluster size >30 vertices) were computed to detect brain regions more involved in at least one experimental condition as compared to the baseline (fixation periods). These cortical maps were computed across subjects (Figure S1a) and in each individual (Figure S1b).

We further examined whether the neural responses of the egomotion regions reflected different velocities of self- (SM) and object-motion (OM). For each of these two motion parameters, we used parametric modulators of the BOLD response. Specifically, the main model contained two multiple parametric modulators (SM and OM), each modeling the absolute velocity (from 0 to 100 km/h in steps of 20 km/h) of the observer and object-motion, respectively. The two parametric modulators were orthogonal with respect to each other, as demonstrated by the absence of a significant correlation between them ($r = .34$; $p = .12$).

We then implemented a different model testing the linear modulation of the BOLD activity as a function of the difference (in absolute value: from 0 to 80 km/h in steps of 20 km/h) between self- and object-motion velocity, reflecting the amount of retinal shift of the object due to the combination of self- and object-motion velocity (retinal motion).

Finally, a representational similarity analysis (RSA; Kriegeskorte et al., 2008) was conducted on multivoxel patterns extracted from the predefined ROIs, starting from estimates of amplitude of the BOLD response elicited by each possible combination of self- and object-motion velocities (21 trials: four different levels of self- and object-motion velocities for each of the five motion conditions +1 static trial). For each subject and for each analyzed region, we extracted the corresponding 21 patterns and computed a neural distance matrix between each possible pair, with neural distance computed as cross-validated Mahalanobis (crossnobis) distances (Diedrichsen et al., 2016; Walther et al., 2016) between the multivoxel patterns. Differently from other distance measures (e.g., Euclidean distance), the crossnobis distance includes a multivariate noise normalization (Arbuckle et al., 2019; Walther et al., 2016) and, provides a meaningful zero point by computing dissimilarities by using a leave-one-out cross-validation scheme. Finally, we computed the correspondence between the neural dissimilarity matrix, that is, the neural distance between the multivoxel patterns elicited by different motion velocities and the "real" dissimilarity, reflecting the actual difference between different motion velocities by using two regression models, separately for self- and object-motion velocities.

3 | RESULTS

We first localized the egomotion areas CSv, pCi, PIC, V6+, V3A, IPSmot/VIP, and MT+ (Figure 2a) by using the flowfield stimulus (see Section 2), and then examined their sensitivity to different visually induced motion conditions including both self- and object-displacements and a combination of them.

We further explored whether the activity of these regions was modulated by the velocity of self and object-motion. To this aim, we
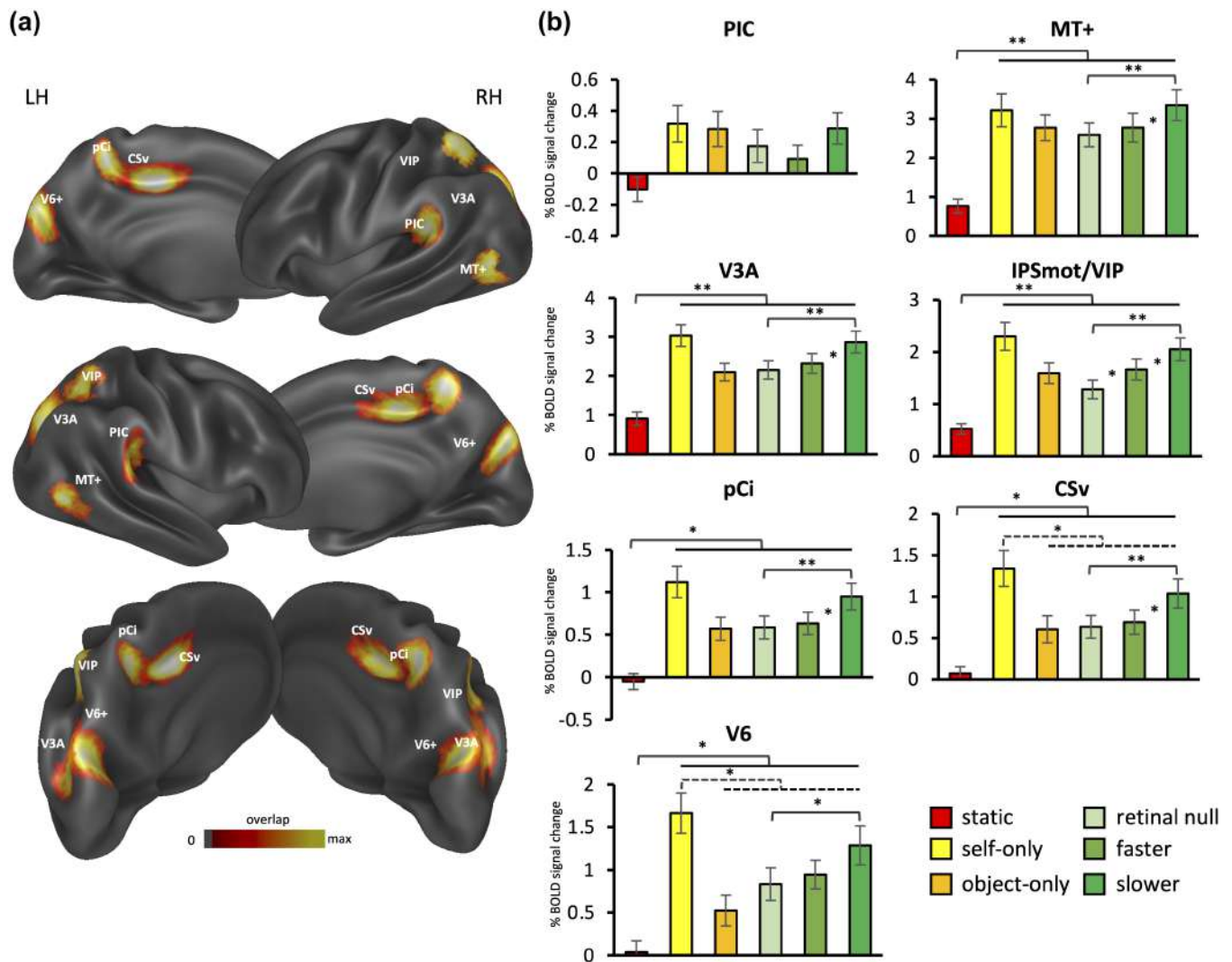
FIGURE 2 Egomotion areas and their sensitivity to translational motion. (a). Brain location of the individually defined egomotion areas CSv, pCi, PIC, V6+, V3A, IPSmot/VIP, and MT+. ROIs are overlapped onto a brain atlas (Conte69) in different views (lateral and medial) of both left (LH) and right (RH) hemispheres. The intensity of color saturation indicates the percentage of participants whose region encompasses that particular node: greater color saturation corresponds to a higher degree of overlap for each node across individual ROIs. (b) ROIs responses are plotted as a function of the experimental condition. Column histograms plot the mean percentage of signal changes (±SE) estimated in each egomotion region and averaged across subjects and hemispheres. *$p < .05$; **$p < .01$. Dashed brackets indicate the preference for pure self-motion over the other motion conditions. Further details about individual data are provided in Figure S2. CSv, cingulate sulcus visual area; pCi, posterior cingulate sulcus area; PIC, posterior insular cortex; ROI, region of interest.

used (1) a parametric modulation analysis to reveal whether the neural activity scaled as a function of the amount of self- and object-motion velocity, and (2) an RSA (Kriegeskorte et al., 2008) to examine whether closer velocities of self- (and object-) motion were associated with activity patterns that exhibited greater similarity in the representational space.

3.1 | Sensitivity to realistic, visually induced translational motion (self, object, and combined)

To clarify whether the egomotion areas CSv, pCi, PIC, V6+, V3A, IPSmot/VIP, and MT+ were sensitive to pure and/or combined self- and

object-motion conditions, we analyzed their response profile as a function of the six different experimental conditions (static, self-only, object-only, retinal-null, object-faster, and object-slower).

Figure 2b shows the mean percent signal change (across the two hemispheres) of each motion region as a function of condition.

In each of these regions, we tested for the presence of reliable activation by using one-sample *t* tests. Results revealed that all motion regions (but PIC) showed a significant and positive response to both self- and object-motion and to a combination of them. Some regions (V3A, IPSmot/VIP, and MT+) also showed a reliable activation for the static condition.

To examine whether these motion regions were differentially activated by the experimental conditions, we submitted the BOLD

signal change of each ROI to a one-way ANOVA, with condition as factor. This analysis revealed a main effect of condition ($5.38 < F_{5,125} < 61.87$; $p < .001$) in all regions, indicating that all of them were differentially activated by the experimental conditions. In particular, we observed that all regions, except bilateral PIC, right V6+, and right CSv, showed a preference for all the five motion conditions (self-only, object-only, retinal-null, object-faster, and object-slower) as compared to the static condition ($p < .017$). By focusing on the preference for the pure motion conditions (self-only and object-only), we observed a preference for the self-only condition only in the left CSv, and in the bilateral V6+ as compared to the other motion conditions ($p < .028$), while no areas showed a preference for the object-motion over the other conditions ($p > .05$).

Among the double-source motion conditions (retinal-null, object-faster, and object-slower), all regions, except PIC, showed a preference for the object-slower (when the object moved slower than the self) as compared to the retinal-null condition, when the self-moved at the same velocity as compared to the object ($p < .006$). Some of these regions (MT+, IPSmot/VIP, CSv, V3A, and right pCi) also showed a preference for the object-slower condition as compared to the object-faster condition ($p < 0.011$). Only left IPSmot/VIP showed a further modulation as a function of the self-to-object relative motion, with higher activity when the object-motion created a retinal slip (object-slower & object-faster > retinal-null; $p < .041$). No areas showed a preference for the object-faster condition over the retinal null condition ($p > .05$).

We finally checked for the presence of any effect related to the motion direction. The paired t tests showed no significant differences between the leftward and rightward directions of motion in any of the tested egomotion ROIs ($t_{25} < 1.65$; $p > .25$).

3.2 | Sensitivity to translational motion in area prostriata

When looking at the whole-brain activation (see Figure S1 and Figure 3), we observed the involvement of the ventral part of the calcarine scissure, at the intersection with the POS, where Mikellidou et al. (2017) have recently identified the human area prostriata, a retinotopic area responsive to extremely fast motion over a wide visual field (see Figure 3a for details about the anatomical position). As done for the egomotion areas, we explored the response profile of area prostriata by using a combination of one-sample t tests, to test the presence of reliable activation, and a one-way ANOVA, with condition as factor, to examine the presence of a differentiated activation across the experimental conditions.

Figure 3b shows the mean percent signal change (across the two hemispheres) in area prostriata as a function of condition. The area showed a significant and positive response to both self- and object-motion and to a combination of them ($p < .005$). Furthermore, the right prostriata showed a sensitivity to the static condition ($p = .0001$). As observed for the egomotion areas, we found a main effect of condition (left prostriata: $F_{5,125} = 21.81$; $p < .0001$; right prostriata: $F_{5,125} = 31.52$; $p < .0001$), indicating that area prostriata was significantly modulated by the experimental conditions. In particular, like CSv and V6+, area prostriata showed a preference for the self-only condition as compared to the other motion conditions ($p < .05$) and for the object-slower condition as compared to the object-faster condition ($p < .05$). In the right hemisphere, we also observed a preference for the object-slower condition as compared to both object-faster ($p = .0001$) and retinal-null condition ($p = .01$). Overall, these results reflected a remarkable preference of the area

FIGURE 3 Whole brain activation map showing the involvement of area prostriata. (a) Group activation map, as resulting from the omnibus F contrast, is displayed on the inflated surface reconstruction (postero-medial view) of atlas Conte69. The MNI coordinates (mm) of the area prostriata are as follows: LH, $x = -20$, $y = -61$, $z = 6$; RH, $x = 22$, $y = -57$, $z = 6$. (b) BOLD response of area prostriata is plotted as a function of the experimental condition. Column histograms plot the mean percentage of signal changes (±SE) averaged across subjects and hemispheres. *$p < .05$; **$p < .01$. Further details about individual data are provided in Figure S2. LH, left hemisphere; RH, right hemisphere.
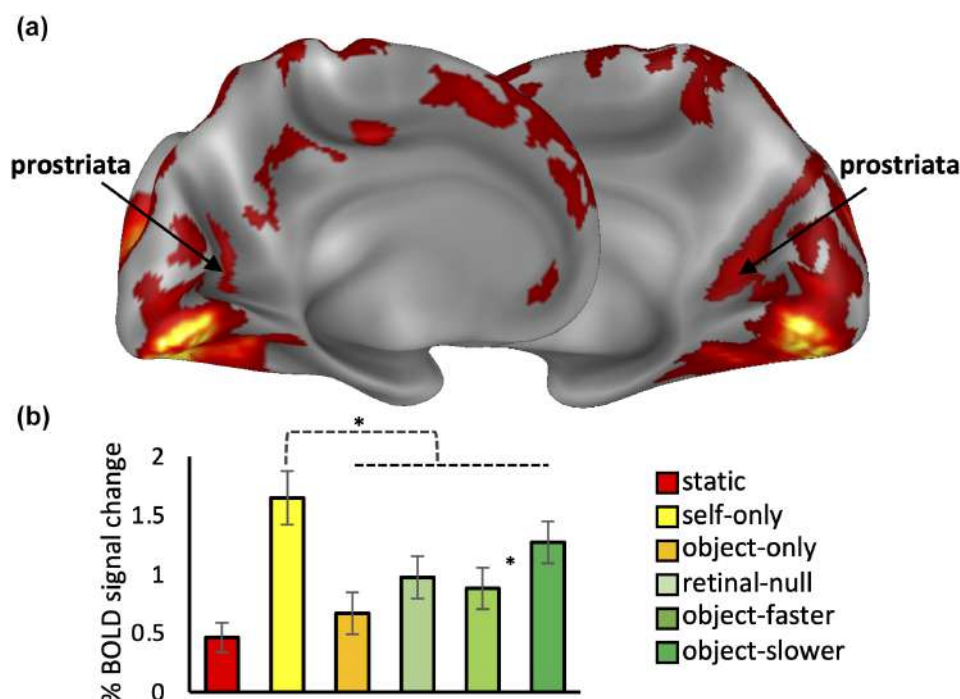
for the self-only condition (as compared to a pure object-motion and to any combination of self- and object-motion) and for a double-source motion condition where the observer moved faster as compared to the object (as compared to the other combinations of self- and object-motion).

3.3 | Impact of motion velocity on neural activity

3.3.1 | Parametric modulation

We further explored whether each egomotion region was significantly modulated by self- and object-motion velocity. To this aim, a parametric analysis of the fMRI data was used to account for the existence of a linear modulation of the BOLD response as a function of the self/object-motion velocity.

A general picture of these effects is shown in Figure 4. When considering the self-motion velocity, we found a significant positive effect, that is, an increase of activity as a function of the amount of simulated self-motion velocity, in all regions ($5.48 < t_{25} < 9.56$; $p < 1$

FIGURE 4 Parametric modulation in the egomotion areas. Plots show the parametric modulation of the BOLD activity as a function of different (self and object) motion velocities. Column histograms plot the impact of parametric modulators reflecting self- (SM) and object-motion (OM) velocities, as measured by the beta weights of these regressors, on the neural activity of each ROI. Asterisks mark significant results. $^{+}p < .05$; Bonferroni-uncorrected; $^{*}p < 1 \times 10^{-4}$; $^{**}p < 1 \times 10^{-5}$. ROI, region of interest.

$\times 10^{-4}$), except PIC. On the other side, we found that object-motion velocity had a significant (and positive) impact on the neural activity only on area MT+ (left: $t_{25} = 2.66$; $p = .013$, Bonferroni-uncorrected; right: $t_{25} = 3.88$; $p = 6.71 \times 10^{-4}$).

To test whether the egomotion regions were further modulated by the relative motion velocity between the observer and the object, we added, in a separate model, a parametric modulator reflecting the retinal motion of the object. We found that the retinal velocity had a significant (and positive) impact on the neural activity in all the investigated regions ($3.48 < t_{25} < 8.93$; $p < 1 \times 10^{-3}$). Being the retinal velocity derived by the other two motion velocities (object- minus self-motion velocity), the observed result likely reflected a modulation effect as a function of the relative motion velocity between the self and the object.

Overall, these results indicate that, although all motion-related regions are modulated by both self-motion and (object-induced) retinal motion velocity, MT is the only area showing an increase of activity as a function of the amount of object-motion velocity.

3.4 | Representational similarity analysis

A second, independent way to test for the presence of neural effects related to motion velocity was the RSA (Kriegeskorte et al., 2008). The idea behind this approach is that closer velocities should evoke more similar distributed neural representations. Thus, RSA was used to test whether similarities between multivoxel patterns reflect different velocities of self (and object) motion.

Figure 5 shows the mean beta values obtained by comparing, through regression models, neural and "real" dissimilarity matrices, separately for self- (Figure 5a) and object-motion (Figure 5b) velocities. We found that different velocities of self-motion significantly predicted neural dissimilarities mainly in areas V6+ (left: $t_{25} = 5.99$, $p = 2.95 \times 10^{-6}$; right: $t_{25} = 5.21$, $p = 2.15 \times 10^{-5}$) and V3A (left: $t_{25} = 5.89$, $p = 8.20 \times 10^{-6}$; right: $t_{25} = 4.57$, $p = 1.14 \times 10^{-4}$), but also, although at a lower extent, in areas MT+ (left: $t_{25} = 3.71$, $p = 1.03 \times 10^{-3}$; right: $t_{25} = 2.86$, $p = .008$ Bonferroni-uncorrected) and CSv (left: $t_{25} = 2.82$; $p = .009$ Bonferroni-uncorrected; right: $t_{25} = 2.93$; $p = 7.13 \times 10^{-3}$). Similarly, different velocities of object-motion strongly predicted neural dissimilarities in areas V6+ (left: $t_{25} = 3.57$, $p = 1.47 \times 10^{-3}$; right: $t_{25} = 3.99$, $p = 5.08 \times 10^{-4}$) and V3A (left: $t_{25} = 4.27$, $p = 2.42 \times 10^{-4}$; right: $t_{25} = 3.35$, $p = 2.57 \times 10^{-3}$) and in area MT+ as well (left: $t_{25} = 3.43$, $p = 2.12 \times 10^{-3}$; right: $t_{25} = 2.75$, $p = .01$ Bonferroni-uncorrected).

Taken together, these results suggest that areas V3A, V6+, and (although at lower extent) MT+ contain a neural representation reflecting the amount of dissimilarity between different self- and object-motion velocities, thus indicating the role of these regions in the fine analysis of these two sources of visual information. Differently for these regions, area CSv was selectively modulated by dissimilarities in terms of self-motion velocities.

Finally, to better characterize how much a given exemplar (i.e., a given stimulus reflecting a specific combination of self- and object-
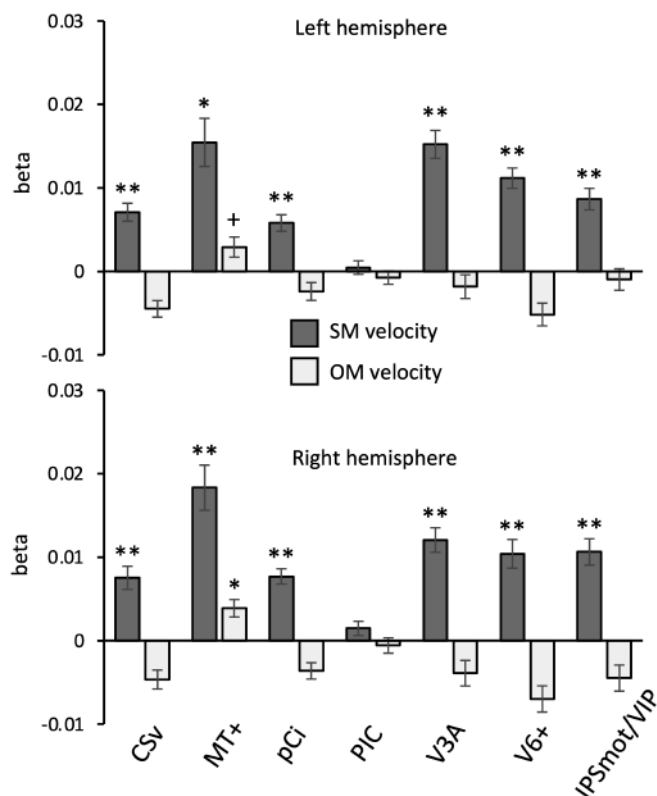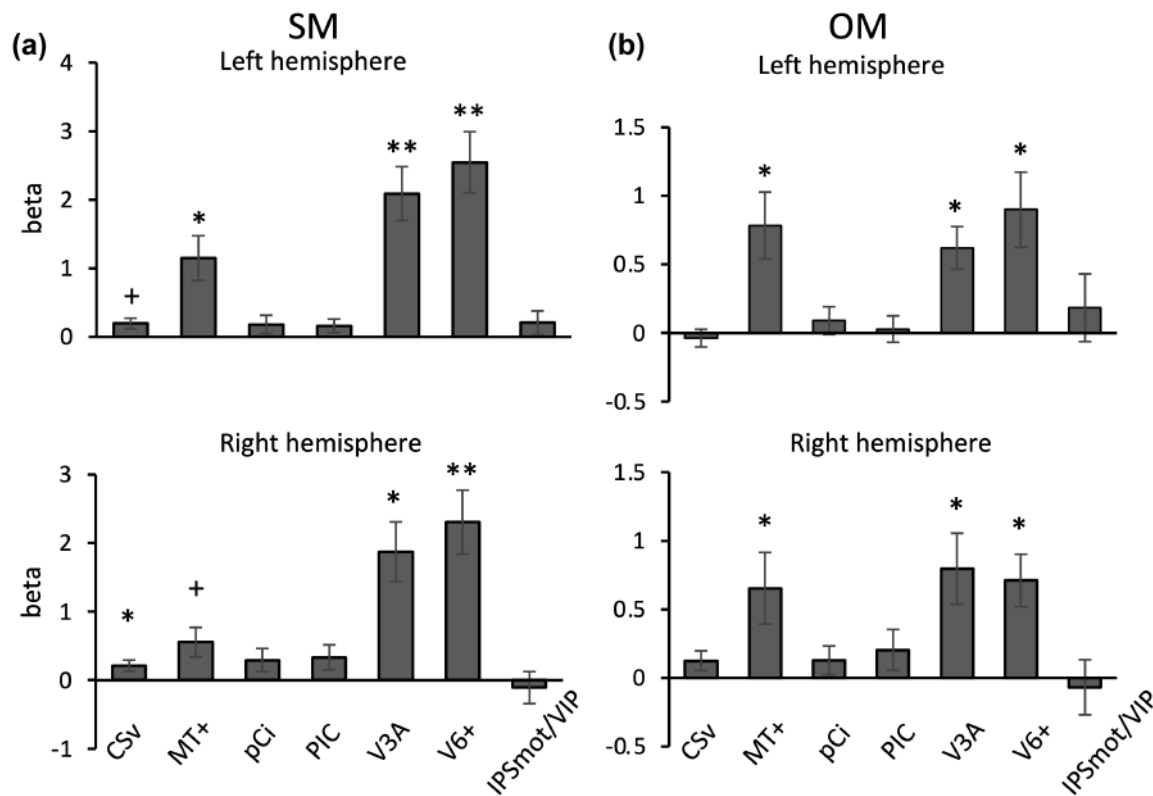
FIGURE 5 Neural dissimilarity in the egomotion areas as a function of motion velocities. Plots show the relationship (as measured by beta weights in the regression model) between the neural dissimilarity and the dissimilarity in terms of self- (a) and object- (b) motion velocity. $^+p < .05$; Bonferroni-uncorrected; $^*p < .001$; $^{**}p < 1 \times 10^{-5}$.

motion velocity) "resembles" another one in terms of the underlying neural representation, we also provided, for each region, the representation dissimilarity matrix (RDM) reflecting the multivariate distances between the neural activation patterns evoked by each pair of stimuli (Figure 6). Among all, areas V6+, V3A, and MT+ showed a remarkable modulation in terms of motion velocities, since greater dissimilarity between different self (and object) motion velocities reflected greater neural dissimilarity (Figure 6, upper panels).

4 | DISCUSSION

In the present study, by combining univariate and multivariate analyses of fMRI data, we set out to establish (1) the sensitivity of several motion-related cortical regions (egomotion regions) to different visually induced motion conditions, including both self- and object-displacements and a combination of them; and (2) whether the activity of these regions was affected by the velocity of both self- and object-motion, thus providing new insight into their role in discriminating between different self- and object-motion velocities, likely with the aim of detecting moving objects. Results show that almost all the egomotion regions showed a reliable response for all motion conditions and were further modulated by the self-motion velocity, while the activity in areas MT, V6, and V3A also reflected different object-motion velocities. We suggest, as explained below, that these

egomotion regions may be involved in the critical computational challenge for detecting scene-relative object-motion.

4.1 | Preference for pure self-motion

One finding of the present study is that CSv (only the left hemisphere) and V6+ (bilaterally) showed a remarkable preference for pure self-motion with respect to pure object-motion and to any combination of self- and object-motion (object-slower, object-faster, and retinal-null). The role of areas CSv and V6 in self-motion processing is well established. Previous findings have shown that CSv is sensitive to wide-field egomotion-compatible stimuli (Antal et al., 2008; Cardin & Smith, 2010; Field et al., 2015; Fischer et al., 2012; Pitzalis, Sdoia, et al., 2013; Wada et al., 2016). Similarly, it has been observed that area CSv did not discriminate different types of optic visual stimulation, if they were all egomotion-compatible, while it was inhibited by the egomotion-incompatible visual motion, as it is the case for random motion (Pitzalis, Sdoia, et al., 2013). More recently, by using a virtual reality fMRI experiment similar to the present study (Pitzalis et al., 2020), we found that CSv responded to all egomotion conditions independently from the presence of object-motion, confirming the suggested role of CSv in self-motion processing (Wall & Smith, 2008).

For what concerns area V6, its role in processing self-motion compatible information is supported by several pieces of evidence.
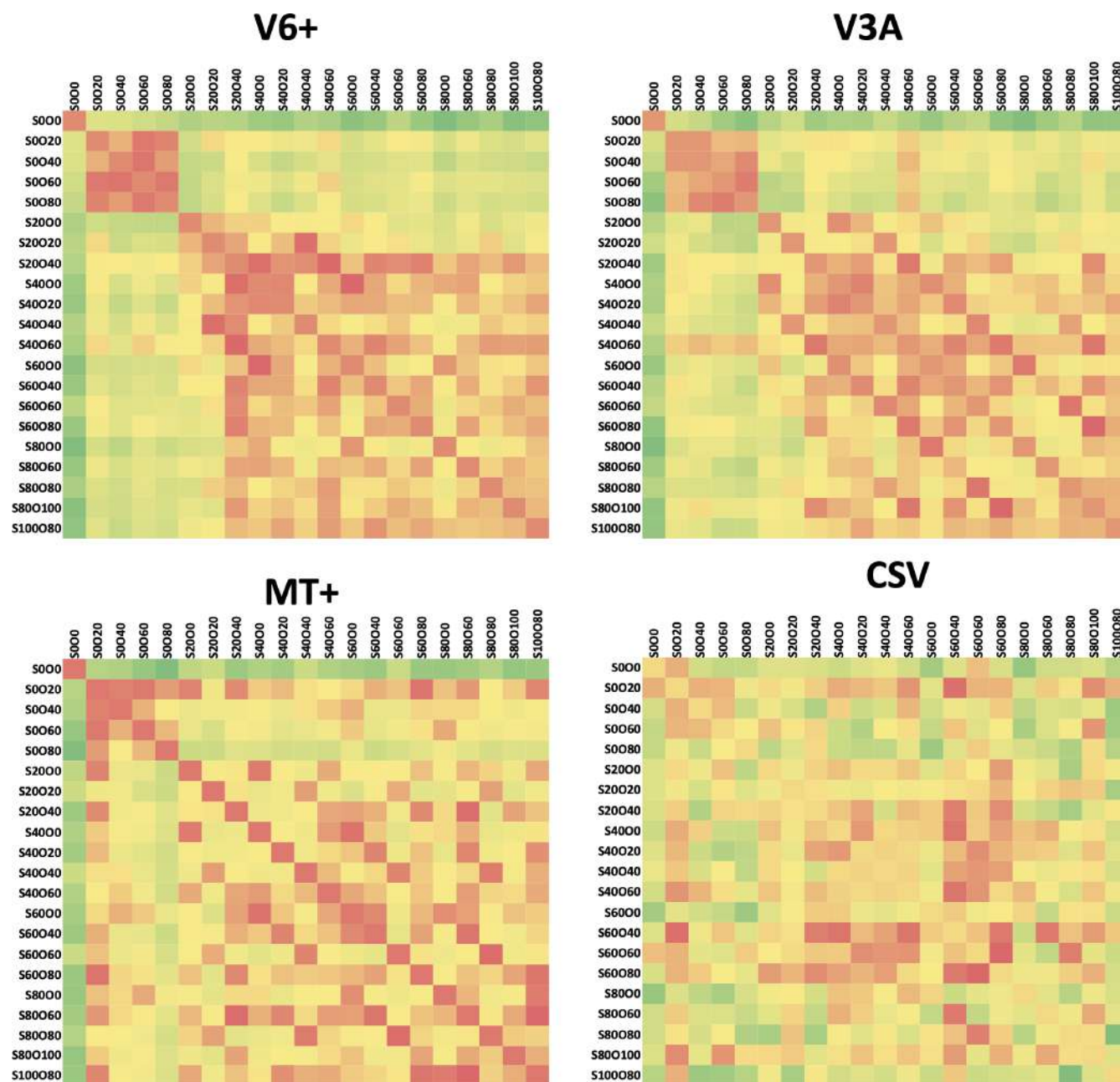
FIGURE 6 Representational dissimilarity matrices reflecting the neural distances (mean crossnobis distances) between pairs of exemplars are plotted in red-to-green patches, for each ROI. RDM is symmetric about a diagonal of zeros. Each exemplar reflects a combination of different velocities of both self (S) and object (O) motion. For example, S20O60 corresponds to a stimulus in which the observer moved at 20 km/h and the object moved at 60 km/h. ROI, region of interest.

For example, it strongly prefers coherent motion over random or incoherent motion (Cardin & Smith, 2010; Helfrich et al., 2013; Pitzalis et al., 2010; von Pföstl et al., 2009), it represents one of the earliest stations (together with MT) processing visual motion coherence, as demonstrated by a study combining visual evoked potentials (VEPs) and fMRI (Pitzalis, Bozzacchi, et al., 2013), and responds to important visual cues that contribute to the perception of self-motion, as changing heading directions (Di Marco, Fattori, et al., 2021; Field et al., 2007; Furlan et al., 2014). In particular, Di Marco, Fattori, et al. (2021) found that the area prefers forward visual motion

(as compared to backward visual motion), suggesting its involvement in a fine visual analysis of the environment toward which the observer is moving during locomotion.

4.2 | Sensitivity to self-motion velocity during complex motion stimulation

A second result of this study is related to the brain sensitivity towards complex motion stimulations including both self- and object-motion.
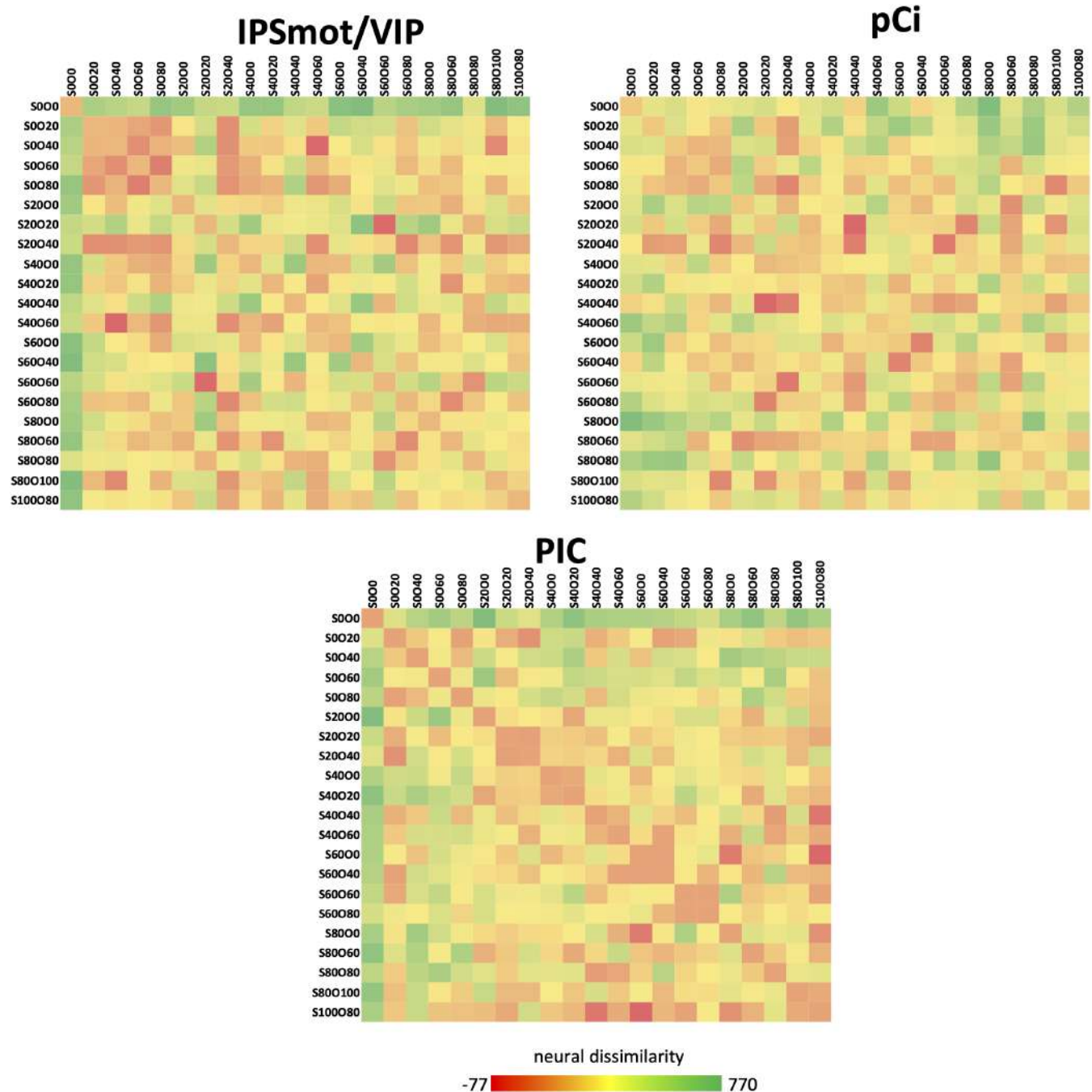
FIGURE 6 (Continued)

Among the double-source motion conditions (retinal-null, object-faster, and object-slower), all regions, except PIC, showed a preference for the object-slower (when the object moved slower than the self) as compared to the retinal-null (when self and object moved at the same velocity and direction). Some of these regions (MT+, V3A, CSv, pCi, and IPSmot/VIP) also showed the preference for the object-slower condition as compared to the object-faster condition (when the object moved faster than the self). Note that object-slower and object-faster conditions differed in self- and object-motion velocities while the retinal motion velocities (and direction) were matched. While in the object-slower condition, the object moved a given amount slower than the self, in the object-faster condition, the relative motion was the opposite (20 km/h in both cases). In other words, keeping constant the object-related retinal motion, the simulated motion of the observer was 20 km/h faster in the object-slower condition. Note that in the object-slower condition, the range of self-motion velocities was 40–100 km/h (mean self-motion velocity: 70 Km/h), while in the object-faster was 20–80 km/h (mean self-motion velocity: 50 Km/h). Thus, the preference we observed for the object-slower condition could be related to the preference of the above-mentioned areas for a relative motion condition where the observer moved (20 km/h) faster than the object as compared to the opposite scenario. It should be

noted that any of the observed effects should be related to a preference for a specific direction of (object-based) retinal motion, which was always opposite to the self-motion direction during the object-slower condition. The absolute motion direction, indeed, could be either leftwards or rightwards, and no significant difference between the two was observed in any of the tested ROIs. This view fits well with the role of these areas in the perception of egomotion-compatible visual motion. The impact of the present results on each of these egomotion regions is described below.

MT+: Although the MT+ role in egomotion is somehow controversial (see Kleinschmidt et al., 2002; Wall & Smith, 2008), more recent lines of evidence seem to re-evaluate its effective importance in terms of perception of egomotion-compatible optic flow. To date, much evidence has been accumulated documenting its involvement in the visual processing of the optic flow associated with self-motion. Since we recently observed that area MT+ shows some degree of preference for egomotion-compatible optic flow (Serra et al., 2019; Sulpizio et al., 2020; Sulpizio et al., 2022), in the present study, we used the flowfield stimulus as a functional localizer of the area. As reported in the method section, the area was successfully identified in almost all the participants to the study, although with a weaker consistency across subjects as compared to the other egomotion regions. Beyond its sensitivity to the coherent optic flow, the present results indicate a prominent role of MT+ in the analysis of self-motion, being the area sensitive to higher self-motion velocities, despite the relative motion information between object and observer was kept constant. Interestingly, we recently observed that the more anterior division of the retinotopically-organized MT cluster (Kolster et al., 2010) responds to both coherent visual motion and lower-limb movements, suggesting its possible involvement in integrating sensory and motor information to perform locomotion (Sulpizio et al., 2022).

V3A: Like area MT, also V3A has a retinotopic organization (Tootell et al., 1997) and its motion sensitivity has been documented in several fMRI studies (Orban et al., 2003; Pitzalis et al., 2010; Sereno et al., 2001; Tootell et al., 1997; Wall & Smith, 2008). Similarly to area MT+, V3A is involved in the processing of motion speed (McKeefry et al., 2008), rotating and radial motion (Harvey et al., 2010), and first-order and second-order motion (Smith et al., 1998). Beyond its sensitivity to the coherent motion (Arnoldussen et al., 2011; Helfrich et al., 2013; Pitzalis et al., 2010; Sereno et al., 2001), area V3A is considered a key region in self-motion processing. It responds to self-motion within a naturalist scene and to a complex visual stimulation including both self- and object-motion (Pitzalis et al., 2020), and shows a preference for the simulated self-motion along the forward (egomotion-compatible) direction (Di Marco, Fattori, et al., 2021), suggesting a fine visual analysis of optic flow generated by locomotion. Here we observed that area V3A showed a preference for higher self-motion velocities during complex motion stimulation, independently of the object-motion velocity. In summary, present results support the view that this motion area is also able to process egomotion signals.

CSv and pCi: The role of the cingulate sulcus (CSv and pCi) in processing egomotion-compatible signals has been confirmed by several recent pieces of evidence. CSv (see also above) has been described as an egomotion-related visual region showing not only high preference for coherent visual motion (Cardin & Smith, 2010; Pitzalis et al., 2020; Serra et al., 2019; Wall & Smith, 2008), but also preference for changes in the direction of self-motion in the environment (Di Marco, Fattori, et al., 2021; Furlan et al., 2014), and for vestibular (Smith et al., 2012) and somatomotor (Serra et al., 2019) stimulation. The pCi exhibits a similar preference for the optic flow stimulus that simulates a locomotion-compatible curved path (Di Marco, Fattori, et al., 2021) and for long-range leg movements (Pitzalis et al., 2019). Additionally, the cortical territory likely including area pCi has been associated with perceiving global motion (Bartels et al., 2008), and notably, vestibular disturbance has been reported in at least one patient with a circumscribed lesion in the precuneus (Wiest et al., 2004). More recently, it has been suggested that area pCi is also involved in the multisensory integration of signals relevant for locomotion, such as visual motion cues and somatomotor signals coming from leg movements (Di Marco, Sulpizio, et al., 2021). Overall, the motion response we observed here in the cingulate sulcus areas further supports the role of CSv and pCi in processing egomotion-compatible signals.

IPSmot/VIP: The parietal area likely corresponding to the macaque VIP (i.e., Bremmer et al., 2001; Duhamel et al., 1998) has been receiving particular attention from recent research on motion perception. Like V6, area VIP can distinguish between different components of optic flow and shows a remarkable response to translational egomotion (Pitzalis, Sdoia, et al., 2013), the same used in the current study. This evidence agrees with the functional role of macaque area VIP, whose neurons exhibit selective responses to optic flow stimuli (Bremmer et al., 2002; Colby et al., 1993) and to the presence of heading direction signals, including the non-visual heading signals available from the vestibular system and other sensory modalities (e.g., Chen et al., 2011; Chen et al., 2013; Zhang & Britten, 2004). The remarkable response of this region for stimuli evoking self-motion sensation is largely confirmed by previous humans (Cardin & Smith, 2010, 2011; Peuskens et al., 2001; Pitzalis, Sdoia, et al., 2013; Sereno & Huang, 2006; Wall & Smith, 2008) and macaque (Bremmer et al., 2001, 2002; Colby et al., 1993) findings suggesting that this area processes several aspects of self-motion. In the present study, we found that the left IPSmot/VIP showed a modulation as a function of self-motion velocity but also as a function of the relative motion between self and object, with higher activity for object-motion generating a retinal slip (object-slower & object-faster > retinal-null). This result seems to agree with the general idea that VIP could use self-motion signals to estimate the self-to-object relative motion, likely with the aim of promoting safety behaviors, such as avoiding obstacles or detecting looming objects (Huang et al., 2012; see also Huang & Sereno, 2018 for a review).

4.3 | Role of area prostriata in self- and object-motion perception

A further interesting result comes from a cortical region, situated at the intersection between the calcarine sulcus and the POS, likely

corresponding to area prostriata, recently described in humans by Mikellidou et al. (2017). This area, which was observed at the whole brain level, showed a high responsiveness to the pure motion condition as compared to the other conditions and was preferentially activated by a complex motion stimulation (combining self- and object-motion) in which the observer moved faster than the object. Area prostriata has been previously described as implicated in processing self-motion within a naturalist scene, with a sensitivity toward a complex visual stimulation including both self- and object-motion (Pitzalis et al., 2020). Overall, these pieces of evidence emphasize the preference of human prostriata for self-motion, thus adding new evidence about the role of this relatively unknown motion-sensitive area in processing visual motion. Future studies may use an individual mapping of the area (i.e., the retinotopic mapping) and motion stimulations combining different velocities of self- and object-motion to better understand its role in processing visual motion velocities.

4.4 | Sensitivity to object-motion velocity: Insight from parametric and multivariate analyses

A key finding of the present study is that almost all the tested regions (but PIC, see below) exhibited a neural modulation as a function of different self-motion velocities, as well as of different velocities of object-induced retinal motion. Interestingly, we observed that only MT+, V6, and V3A were further modulated by the world-relative object-motion velocity. In particular, results from the parametric analysis revealed the existence of a linear relationship between the activity of MT+ and increasing object-motion velocities. Also, the RSA (Kriegeskorte et al., 2008) on this region revealed that the multivoxel pattern of activity was organized as reflecting the different object-motion velocities. Considering that a way to detect moving objects is using their speed (Royden & Moore, 2012), the MT+ sensitivity towards object-motion velocity could be an index of "real" motion detection. Interestingly, "real motion cells" (for a review, see Galletti & Fattori, 2003) have been found in many regions of the visual stream, including areas MT/V5 (Erickson & Their, 1991) and MST (Erickson & Their, 1991). Present results also agree with computation models based on MT-like operators. For example, Royden and Holloway (2014) demonstrated that a model using speed- and direction-tuned units, whose responses are modeled on the functional properties of the macaque MT neurons, is able to successfully detect the borders of moving objects within a scene as the observer moves through it. In a recent study based on visual motion stimulation within a realistic scene (Pitzalis et al., 2020), similar to that used in the present study, we observed that area MT+, together with other cortical regions including V6 and V3A (see below), was able to extract object-motion information from the overall motion. However, because in the above-mentioned study, the velocity of object (and self) was constant (always 60 km/h), present results add a piece of knowledge on how MT+ may accomplish the critical computations required to detect scene-relative object-motion.

Besides area MT, "real motion" cells have been also found in the monkey areas V1, V2, V3A, and V6 (Galletti et al., 1984, 1988, 1990; Galletti & Fattori, 2003), with the higher percentage in areas V3A and V6 (see Galletti & Fattori, 2003 for a review). In humans, along the same line of evidence, recent fMRI data have revealed that areas V6 and V3A can infer "real" motion after discarding self-induced retinal motion. Fischer et al. (2012) demonstrated that both V6 and V3A ensure perceptual stability despite eye movements. By using a similar task, Nau et al. (2018) showed that areas V6 and V3A can differentiate between distinct velocities of objective motion during pursuit, thus supporting the integration between the direction of retinal motion and that of eye movements. Compatible with this view, present data suggest that areas V6+ and V3A contain a neural representation reflecting not only different self-motion velocities but also different object-motion velocities, being the pattern of neural activity more similar for closer motion velocities. Differently from area MT+, both V6+ and V3A did not exhibit a linear increase of activation as a function of the amount of object-motion velocity, as highlighted by the parametric analysis, likely indicating that the sensitivity to different object-motion velocities was related to the information extracting from their (multivoxel) activity pattern. An open question remains to characterize how information provided by univariate and multivariate techniques might integrate for a better understanding of the investigated mental state. Overall, as hypothesized for area MT+, the object-motion sensitivity observed in the activity pattern of areas V6+ and V3A may speak in favor of their involvement in implementing the neural computations (i.e., discounting of the self-induced retinal motion) required to detect object-motion during self-motion. We thus suggest that the functional profile exhibited by MT+, V6+, and V3A should provide the potential substrate for some discounting processes, like flow parsing, allowing for the estimation of scene-relative object velocity. Future studies may address the relative contribution of these areas in performing these critical computations.

4.5 | Role of PIC in self- and object-motion perception

A final note goes to the absence of a remarkable motion-selective response in area PIC. The area did not show any kind of neural modulation as a function of the amount of both self- and object-motion velocities. Additionally, its sensitivity to the motion conditions was often modest, especially in the left hemisphere. While the right PIC showed a positive response (significant and Bonferroni-corrected) in both pure self- and object-motion and in retinal-motion condition, the left PIC showed a significant, but Bonferroni-uncorrected, response for the two pure motion conditions. In literature, the right (but not the left) PIC has been suggested as having a role in sensing and guiding translational egomotion (Huang et al., 2015). More recently, we found that only the right PIC was activated by a visual motion stimulation including self- and object-motion and a combination of them (Pitzalis et al., 2020). Since area PIC is known as a multisensory region

responding not only to visual (Frank et al., 2014, 2016), but also to vestibular (Fasold et al., 2002; Smith et al., 2012) motion, the discrepancy observed in the current and in previous studies is consistent with the dominance of the right vestibular cortex in right-handed subjects, as highlighted by previous neuroimaging studies using a combination of vestibular, optokinetic, and visual stimuli (Dieterich et al., 1998; Dieterich et al., 2003). Thus, the absence of a clear involvement of area PIC in the experimental paradigm used in the present study could be related to the lack of a vestibular stimulation in our experimental conditions. Area PIC is thought to mainly support integration processes between visual and vestibular cues (Frank et al., 2016) and between visual and somatomotor cues (Di Marco, Sulpizio, et al., 2021), likely with the aim of promoting self-motion perception during locomotion, and both are absent in our experimental conditions.

5 | CONCLUSION

In the present study, a differentiated profile emerges among the egomotion regions during a visual motion stimulation including self- and object-displacements and a combination of them. We found that all the egomotion regions (except area PIC) showed a reliable activation for all the visual motion conditions and were further modulated by the self-motion velocity. Interestingly, areas MT+, V6+, and V3A also showed a response profile reflecting different object-motion velocities.

Apart from providing an overview on the role of each cortical node of the egomotion network in encoding different combinations of self- and object-motion, the current study, by manipulating the relative motion velocity between the observer (the self) and the object within a stationary scene, points to reveal the neural signature of the complex computation required for detecting scene-relative object-motion during self-motion. We propose that crucial nodes of the dorsal visual system, such as MT+, V6+, and V3A, are fundamental to implement such a critical computation.

CONFLICT OF INTEREST STATEMENT
The authors declare no conflicts of interest.

DATA AVAILABILITY STATEMENT
The authors have documented all data, methods, and materials used to conduct this research study, and anonymized data will be shared by request from any qualified investigator.

ORCID
Valentina Sulpizio https://orcid.org/0000-0001-7000-550X
Gaspare Galati https://orcid.org/0000-0002-0640-4247
Sabrina Pitzalis https://orcid.org/0000-0002-4445-0391

REFERENCES
Antal, A., Baudewig, J., Paulus, W., & Dechent, P. (2008). The posterior cingulate cortex and planum temporale/parietal operculum are activated by coherent visual motion. *Visual Neuroscience*, 25(1), 17–26. https://doi.org/10.1017/S0952523808080024

Arbuckle, S., Yokoi, A., Pruszynski, J. A., & Diedrichsen, J. (2019). Stability of representational geometry across a wide range of fMRI activity levels. *NeuroImage*, 186, 155–163. https://doi.org/10.1101/266585

Arnoldussen, D. M., Goossens, J., & van den Berg, A. V. (2011). Adjacent visual representations of self-motion in different reference frames. *Proceedings of the National Academy of Sciences of the United States of America*, 108(28), 11668–11673. https://doi.org/10.1073/pnas.1102984108

Bartels, A., Zeki, S., & Logothetis, N. K. (2008). Natural vision reveals regional specialization to local motion and to contrast-invariant, global flow in the human brain. *Cerebral Cortex*, 18(3), 705–717. https://doi.org/10.1093/cercor/bhm107

Bremmer, F., Duhamel, J. R., Ben Hamed, S., & Graf, W. (2002). Heading encoding in the macaque ventral intraparietal area (VIP). *European Journal of Neuroscience*, 16(8), 1554–1568. https://doi.org/10.1046/j.1460-9568.2002.02207.x

Bremmer, F., Schlack, A., Shah, N. J., Zafiris, O., Kubischik, M., Hoffmann, K. P., & Fink, G. R. (2001). Polymodal motion processing in posterior parietal and premotor cortex. *Neuron*, 29, 287–296. https://doi.org/10.1016/s0896-6273(01)00198-2

Bridgeman, B. (1973). Receptive fields in single cells of monkey visual cortex during visual tracking. *The International Journal of Neuroscience*, 6, 141–152. https://doi.org/10.3109/00207457309147657

Calabro, F. J., & Vaina, L. M. (2012). Interaction of cortical networks mediating object-motion detection by moving observers. *Experimental Brain Research*, 221(2), 177–189.

Cardin, V., & Smith, A. T. (2010). Sensitivity of human visual and vestibular cortical regions to egomotion-compatible visual stimulation. *Cerebral Cortex*, 20(8), 1964–1973.

Cardin, V., & Smith, A. T. (2011). Sensitivity of human visual cortical area V6 to stereoscopic depth gradients associated with self-motion. *Journal of Neurophisiology*, 106, 1240–1249. https://doi.org/10.1152/jn.01120.2010

Chen, A., DeAngelis, G. C., & Angelaki, D. E. (2011). Representation of vestibular and visual cues to self-motion in ventral intraparietal cortex. *The Journal of Neuroscience*, 31, 12036–12052. https://doi.org/10.1523/JNEUROSCI.0395-11.2011

Chen, A., DeAngelis, G. C., & Angelaki, D. E. (2013). Functional specializations of the ventral intraparietal area for multisensory heading discrimination. *The Journal of Neuroscience*, 33, 3567–3581. https://doi.org/10.1523/JNEUROSCI.4522-12.2013

Colby, C. L., Duhamel, J. R., & Goldberg, M. E. (1993). Ventral intraparietal area of the macaque: Anatomic location and visual response properties. *Journal of Neurophysiology*, 69(3), 902–914. https://doi.org/10.1152/jn.1993.69.3.902

Cox, R. W., & Hyde, J. S. (1997). Software tools for analysis and visualization of fMRI data. *NMR in Biomedicine*, 10(4–5), 171–178. https://doi.org/10.1002/(SICI)1099-1492(199706/08)10:4/5<171::AID-NBM453>3.0.CO;2-L

Dale, A. M., Fischl, B., & Sereno, M. I. (1999). Cortical surface-based analysis: I. Segmentation and surface reconstruction. *NeuroImage*, 9(2), 179–194. https://doi.org/10.1006/nimg.1998.0395

Di Marco, S., Fattori, P., Galati, G., Galletti, C., Lappe, M., Maltempo, T., & Pitzalis, S. (2021). Preference for locomotion-compatible curved paths and forward direction of self-motion in somato-motor and visual areas. *Cortex*, *137*, 74–92.

Di Marco, S., Sulpizio, V., Bellagamba, M., Fattori, P., Galati, G., Galletti, C., & Pitzalis, S. (2021). Multisensory integration in cortical regions responding to locomotion-related visual and somato-motor signals. *NeuroImage*, *244*, 118581. https://doi.org/10.1016/j.neuroimage.2021.118581

Diedrichsen, J., Provost, S., & Zareamoghaddam, H. (2016). On the distribution of cross-validated Mahalanobis distances. *arXiv:1607.01371*. https://doi.org/10.48550/arXiv.1607.0137

Dieterich, M., Bense, S., Lutz, S., Drzezga, A., Stephan, T., Bartenstein, P., & Brandt, T. (2003). Dominance for vestibular cortical function in the non-dominant hemisphere. *Cerebral Cortex*, *13*, 994–1007. https://doi.org/10.1093/cercor/13.9.994

Dieterich, M., Bucher, S. F., Seelos, K. C., & Brandt, T. (1998). Horizontal or vertical optokinetic stimulation activates visual motion-sensitive, ocu-Lar motor and vestibular cortex areas with right hemispheric dominance. An fMRI study. *Brain*, *121*, 1479–1495. https://doi.org/10.1093/brain/121.8.1479

Duffy, C. J. (1998). MST neurons respond to optic flow and translational movement. *Journal of Neurophysiology*, *80*(4), 1816–1827. https://doi.org/10.1152/jn.1998.80.4.1816

Duhamel, J. R., Colby, C. L., & Goldberg, M. E. (1998). Ventral intraparietal area of the macaque: Congruent visual and somatic response properties. *Journal of Neurophysiology*, *79*(1), 126–136. https://doi.org/10.1234/12345678

Erickson, R. G., & Their, P. (1991). A neuronal correlate of spatial stability during periods of self-induced visual motion. *Experimental Brain Research*, *86*, 608–616.

Esteban, O., Markiewicz, C. J., Blair, R. W., Moodie, C. A., Isik, A. I., Erramuzpe, A., Kent, J. D., Goncalves, M., DuPre, E., Snyder, M., Oya, H., Ghosh, S. S., Wright, J., Durnez, J., Poldrack, R. A., & Gorgolewski, K. J. (2018). fMRIPrep: A robust preprocessing pipeline for functional MRI. *Nature Methods*, *16*, 111–116. https://doi.org/10.1038/s41592-018-0235-4

Fasold, O., von Brevern, M., Kuhberg, M., Ploner, C. J., Villringer, A., Lempert, T., & Wenzel, R. (2002). Human vestibular cortex as identified with caloric stimulation in functional magnetic resonance imaging. *NeuroImage*, *17*(3), 1384–1393. https://doi.org/10.1006/nimg.2002.1241

Faul, F., Erdfelder, E., Lang, A. G., & Buchner, A. (2007). G*Power 3: A flexible statistical power analysis program for the social, behavioral, and biomedical sciences. *Behavior Research Methods*, *39*, 175–191. https://doi.org/10.3758/bf03193146

Field, D. T., Inman, L. A., & Li, L. (2015). Visual processing of optic flow and motor control in the human posterior cingulate sulcus. *Cortex*, *71*, 377–389.

Field, D. T., Wilkie, R. M., & Wann, J. P. (2007). Neural systems in the visual control of steering. *The Journal of Neuroscience*, *27*(30), 8002–8010.

Fischer, E., Bülthoff, H. H., Logothetis, N. K., & Bartels, A. (2012). Human areas V3A and V6 compensate for self-induced planar visual motion. *Neuron*, *73*, 1228–1240. https://doi.org/10.1016/j.neuron.2012.01.022

Frank, S. M., Baumann, O., Mattingley, J. B., & Greenlee, M. W. (2014). Vestibular and visual responses in human posterior insular cortex. *Journal of Neurophysiology*, *112*(10), 2481–2491. https://doi.org/10.1152/jn.00078.2014

Frank, S. M., Wirth, A. M., & Greenlee, M. W. (2016). Visual-vestibular processing in the human Sylvian fissure. *Journal of Neurophysiology*, *116*(2), 263–271. https://doi.org/10.1152/jn.00009.2016

Furlan, M., Wann, J. P., & Smith, A. T. (2014). A representation of changing heading direction in human cortical areas pVIP and CSv. *Cerebral Cortex*, *24*(11), 2848–2858. https://doi.org/10.1093/cercor/bht132

Galletti, C., Battaglini, P. P., & Aicardi, G. (1988). 'Real-motion' cells in visual area V2 of behaving macaque monkeys. *Experimental Brain Research*, *69*(2), 279–288. https://doi.org/10.1007/BF00230838

Galletti, C., Battaglini, P. P., & Fattori, P. (1990). "Real-motion" cells in area V3A of macaque visual cortex. *Experimental Brain Research*, *82*(1), 67–76. https://doi.org/10.1007/BF00230838

Galletti, C., & Fattori, P. (2003). Neuronal mechanisms for detection of motion in the field of view. *Neuropsychologia*, *41*(13), 1717–1727.

Galletti, C., Fattori, P., Battaglini, P. P., Shipp, S., & Zeki, S. (1996). Functional demarcation of a border between areas V6 and V6A in the superior parietal gyrus of the macaque monkey. *The European Journal of Neuroscience*, *8*, 30–52.

Galletti, C., Fattori, P., Gamberini, M., & Kutz, D. F. (1999). The cortical visual area V6: Brain location and visual topography. *The European Journal of Neuroscience*, *11*, 3922–3936.

Galletti, C., Squatrito, S., Battaglini, P. P., & Grazia Maioli, M. (1984). 'Real-motion' cells in the primary visual cortex of macaque monkeys. *Brain Research*, *301*(1), 95–110. https://doi.org/10.1016/0006-8993(84)90406-2

Gibson, J. J. (1950). *The perception of the visual world*. Houghton Mifflin.

Glasser, M. F., Sotiropoulos, S. N., Wilson, J. A., Coalson, T. S., Fischl, B., Andersson, J. L., Xu, J., Jbabdi, S., Webster, M., Polimeni, J. R., van Essen, D., Jenkinson, M., & WU-Minn HCP Consortium. (2013). The minimal preprocessing pipelines for the human connectome project. *NeuroImage*, *80*, 105–124. https://doi.org/10.1016/j.neuroimage.2013.04.127

Gorgolewski, K., Burns, C. D., Madison, C., Clark, D., Halchenko, Y. O., Waskom, M. L., & Ghosh, S. (2011). Nipype: A flexible, lightweight and extensible neuroimaging data processing framework in Python. *Frontiers in Neuroinformatics*, *5*, 13. https://doi.org/10.3389/fninf.2011.00013

Greenlee, M. W., Frank, S. M., Kaliuzhna, M., Blanke, O., Bremmer, F., Churan, J., Cuturi, L. F., MacNeilage, P. R., & Smith, A. T. (2016). Multisensory integration in self motion perception. *Multisensory Research*, *29*(6–7), 525–556. https://doi.org/10.1163/22134808-00002527

Greve, D. N., & Fischl, B. (2009). Accurate and robust brain image alignment using boundary-based registration. *NeuroImage*, *48*(1), 63–72. https://doi.org/10.1016/j.neuroimage.2009.06.060

Harvey, B. M., Braddick, O. J., & Cowey, A. (2010). Similar effects of repetitive transcranial magnetic stimulation of MT+ and a dorsomedial extrastriate site including V3A on pattern detection and position discrimination of rotating and radial motion patterns. *Journal of Vision*, *10*(5), 21.

Helfrich, R. F., Becker, H. G., & Haarmeier, T. (2013). Processing of coherent visual motion in topographically organized visual areas in human cerebral cortex. *Brain Topography*, *26*(2), 247–263. https://doi.org/10.1007/s10548-012-0226-1

Huang, R., & Sereno, M. I. (2018). Multisensory and sensorimotor maps. In *The parietal lobe* (1st ed.). Elsevier B.V.

Huang, R. S., Chen, C., Tran, A. T., Holstein, K. L., & Sereno, M. I. (2012). Mapping multisensory parietal face and body areas in humans. *Proceedings of the National Academy of Sciences of the United States of America*, *109*(44), 18114–18119. https://doi.org/10.1073/pnas.1207946109

Huang, R. S., Chen, C. F., & Sereno, M. I. (2015). Neural substrates underlying the passive observation and active control of translational egomotion. *The Journal of Neuroscience*, *35*, 4258–4267. https://doi.org/10.1523/JNEUROSCI.2647-14.2015

Jenkinson, M., Bannister, P., Brady, M., & Smith, S. (2002). Improved optimization for the robust and accurate linear registration and motion correction of brain images. *NeuroImage*, *17*(2), 825–841. https://doi.org/10.1006/nimg.2002.1132

Kim, H. R., Angelaki, D. E., & DeAngelis, G. C. (2016). The neural basis of depth perception from motion parallax. *Philosophical Transactions of the Royal Society B*, 371, 20150256.

Kim, H. R., Angelaki, D. E., & DeAngelis, G. C. (2022). A neural mechanism for detecting object motion during self-motion. *eLife*, 11, e74971. https://doi.org/10.7554/eLife.74971

Klein, A., Ghosh, S. S., Bao, F. S., Giard, J., Häme, Y., Stavsky, E., Lee, N., Rossa, B., Reuter, M., Chaibub Neto, E., & Keshavan, A. (2017). Mind-boggling morphometry of human brains. *PLoS Computational Biology*, 13(2), e1005350. https://doi.org/10.1371/journal.pcbi.1005350

Kleinschmidt, A., Thilo, K. V., Büchel, C., Gresty, M. A., Bronstein, A. M., & Frackowiak, R. S. (2002). Neural correlates of visual-motion perception as object- or self-motion. *NeuroImage*, 16(4), 873–882. https://doi.org/10.1006/nimg.2002.1181

Kolster, H., Peeters, R., & Orban, G. A. (2010). The retinotopic organization of the human middle temporal area MT/V5 and its cortical neighbors. *The Journal of Neuroscience*, 30(29), 9801–9820.

Kriegeskorte, N., Mur, M., Ruff, D. A., Kiani, R., Bodurka, J., Esteky, H., Tanaka, K., & Bandettini, P. A. (2008). Matching categorical object representations in inferior temporal cortex of man and monkey. *Neuron*, 60, 1126–1141. https://doi.org/10.1016/j.neuron.2008.10.043

Kwong, K. K., Belliveau, J. W., Chesler, D. A., Goldberg, I. E., Weisskoff, R. M., Poncelet, B. P., & Turner, R. (1992). Dynamic magnetic resonance imaging of human brain activity during primary sensory stimulation. *Proceedings of the National Academy of Sciences of the United States of America*, 89(12), 5675–5679. https://doi.org/10.1073/pnas.89.12.5675

Mangan, A. P., & Whitaker, R. T. (1999). Partitioning 3D surface meshes using watershed segmentation. *IEEE Transactions on Visualization and Computer Graphics*, 5(4), 308–321. https://doi.org/10.1109/2945.817348

McKeefry, D. J., Burton, M. P., Vakrou, C., Barrett, B. T., & Morland, A. B. (2008). Induced deficits in speed perception by transcranial magnetic stimulation of human cortical areas V5/MT+ and V3A. *Journal of Neuroscience*, 28(27), 6848–6857.

Mikellidou, K., Kurzawski, J. W., Frijia, F., Montanaro, D., Greco, V., Burr, D. C., & Morrone, M. C. (2017). Area prostriata in the human brain. *Current Biology*, 27(19), 3056–3060.e3. https://doi.org/10.1016/j.cub.2017.08.065

Morrone, M. C., Tosetti, M., Montanaro, D., Fiorentini, A., Cioni, G., & Burr, D. C. (2000). A cortical area that responds specifically to optic flow, revealed by fMRI. *Nature Neuroscience*, 3, 1322–1328. https://doi.org/10.1038/81860

Nadler, J. W., Barbash, D., Kim, H. R., Shimpi, S., Angelaki, D. E., & Deangelis, G. C. (2013). Joint representation of depth from motion parallax and binocular disparity cues in macaque area MT. *The Journal of Neuroscience*, 33, 14061–14074.

Nau, M., Schindler, A., & Bartels, A. (2018). Real-motion signals in human early visual cortex. *NeuroImage*, 175, 379–387. https://doi.org/10.1016/j.neuroimage.2018.04.012

Oldfield, R. C. (1971). The assessment and analysis of handedness: The Edinburgh inventory. *Neuropsychologia*, 9, 97–113. https://doi.org/10.1016/0028-3932(71)90067-4

Orban, G. A., Fize, D., Peuskens, H., Denys, K., Nelissen, K., Sunaert, S., Todd, J., & Vanduffel, W. (2003). Similarities and differences in motion processing between the human and macaque brain: Evidence from fMRI. *Neuropsychologia*, 41, 1757–1768.

Peuskens, H., Sunaert, S., Dupont, P., Van Hecke, P., & Orban, G. A. (2001). Human brain regions involved in heading estimation. *The Journal of Neuroscience*, 21(7), 2451–2461. https://doi.org/10.1523/JNEUROSCI.21-07-02451.2001

Pitzalis, S., Bozzacchi, C., Bultrini, A., Fattori, P., Galletti, C., & Di Russo, F. (2013). Parallel motion signals to the medial and lateral motion areas V6 and MT+. *NeuroImage*, 67, 89–100. https://doi.org/10.1016/j.neuroimage.2012.11.022

Pitzalis, S., Fattori, P., & Galletti, C. (2013). The functional role of the medial motion area V6. *Frontiers in Behavioral Neuroscience*, 6, 91.

Pitzalis, S., Galletti, C., Huang, R. S., Patria, F., Committeri, G., Galati, G., & Sereno, M. I. (2006). Wide-field retinotopy defines human cortical visual area V6. *Journal of Neuroscience*, 26(30), 7962–7973. https://doi.org/10.1523/JNEUROSCI.0178-06.2006

Pitzalis, S., Hadj-Bouziane, F., Dal Bò, G., Guedj, C., Strappini, F., Meunier, M., & Galletti, C. (2021). Optic flow selectivity in the macaque parieto-occipital sulcus. *Brain Structure and Function*, 226, 2911–2930. https://doi.org/10.1007/s00429-021-02293-w

Pitzalis, S., Sdoia, S., Bultrini, A., Committeri, G., Di Russo, F., Fattori, P., & Galati, G. (2013). Selectivity to translational egomotion in human brain motion areas. *PLoS One*, 8(4), e60241.

Pitzalis, S., Sereno, M. I., Committeri, G., Fattori, P., Galati, G., Patria, F., & Galletti, C. (2010). Human V6: The medial motion area. *Cerebral Cortex*, 20(2), 411–424.

Pitzalis, S., Sereno, M. I., Committeri, G., Fattori, P., Galati, G., Tosoni, A., & Galletti, C. (2013). The human homologue of macaque area V6A. *NeuroImage*, 82, 517–530. https://doi.org/10.1016/j.neuroimage.2013.06.026

Pitzalis, S., Serra, C., Sulpizio, V., Committeri, G., de Pasquale, F., Fattori, P., Galletti, C., Sepe, R., & Galati, G. (2020). Neural bases of self- and object-motion in a naturalistic vision. *Human Brain Mapping*, 41, 1084–1111. https://doi.org/10.1002/hbm.24862

Pitzalis, S., Serra, C., Sulpizio, V., Di Marco, S., Fattori, P., Galati, G., & Galletti, C. (2019). A putative human homologue of the macaque area PEc. *NeuroImage*, 202, 116092.

Power, J. D., Mitra, A., Laumann, T. O., Snyder, A. Z., Schlaggar, B. L., & Petersen, S. E. (2014). Methods to detect, characterize, and remove motion artifact in resting state fMRI. *NeuroImage*, 84(Suppl C), 320–341. https://doi.org/10.1016/j.neuroimage.2013.08.048

Raffi, M., Squatrito, S., & Maioli, M. G. (2002). Neuronal responses to optic flow in the monkey parietal area PEc. *Cerebral Cortex*, 12, 639–646.

Royden, C. S., & Holloway, M. A. (2014). Detecting moving objects in an optic flow field using direction- and speed-tuned operators. *Vision Research*, 98, 14–25. https://doi.org/10.1016/j.visres.2014.02.009

Royden, C. S., & Moore, K. D. (2012). Use of speed cues in the detection of moving objects by moving observers. *Vision Research*, 59, 17–24. https://doi.org/10.1016/j.visres.2012.02.006

Rushton, S. K., & Warren, P. A. (2005). Moving observers, relative retinal motion and the detection of object movement. *Current Biology*, 15(14), R542–R543. https://doi.org/10.1016/j.cub.2005.07.020

Sakata, H., Shibutan, H., Kawano, K., & Harrington, T. L. (1985). Neural mechanisms of space vision in the parietal association cortex of the monkey. *Vision Research*, 25, 453–463. https://doi.org/10.1016/0042-6989(85)90070-7

Schindler, A., & Bartels, A. (2018a). Human V6 integrates visual and extra-retinal cues during head-induced gaze shifts. *iScience*, 7, 191–197. https://doi.org/10.1016/j.isci.2018.09.004

Schindler, A., & Bartels, A. (2018b). Integration of visual and non-visual self-motion cues during voluntary head movements in the human brain. *NeuroImage*, 172, 597–607. https://doi.org/10.1016/j.neuroimage.2018.02.006

Sereno, M. I., & Huang, R. S. (2006). A human parietal face area contains aligned head-centered visual and tactile maps. *Nature Neuroscience*, 9, 1337–1343. https://doi.org/10.1038/nn1777

Sereno, M. I., Pitzalis, S., & Martinez, A. (2001). Mapping of contralateral space in retinotopic coordinates by a parietal cortical area in humans. *Science*, 294(5545), 1350–1354. https://doi.org/10.1126/science.1063695

Serra, C., Galletti, C., Di Marco, S., Fattori, P., Galati, G., Sulpizio, V., & Pitzalis, S. (2019). Egomotion-related visual areas respond to active leg movements. *Human Brain Mapping*, 40, 3174–3191. https://doi.org/10.1002/hbm.24589

Smith, A. T., Greenlee, M. W., Singh, K. D., Kraemer, F. M., & Hennig, J. (1998). The processing of first- and second-order motion in human visual cortex assessed by functional magnetic resonance imaging (fMRI). *The Journal of Neuroscience*, 18, 3816–3830. https://doi.org/10.1523/JNEUROSCI.18-10-03816.1998

Smith, A. T., Wall, M. B., & Thilo, K. V. (2012). Vestibular inputs to human motion-sensitive visual cortex. *Cerebral Cortex*, 22(5), 1068–1077. https://doi.org/10.1093/cercor/bhr179

Sulpizio, V., Fattori, P., Pitzalis, S., & Galletti, C. (2023). Functional organization of the caudal part of the human superior parietal lobule. *Neuroscience and Biobehavioral Reviews*, 153, 105357. https://doi.org/10.1016/j.neubiorev.2023.105357

Sulpizio, V., Galati, G., Fattori, P., Galletti, C., & Pitzalis, S. (2020). A common neural substrate for processing scenes and egomotion-compatible visual motion. *Brain Structure & Function*, 225(7), 2091–2110.

Sulpizio, V., Strappini, F., Fattori, P., Galati, G., Galletti, C., Pecchinenda, A., & Pitzalis, S. (2022). The human middle temporal cortex responds to both active leg movements and egomotion-compatible visual motion. *Brain Structure & Function*, 227(8), 2573–2592. https://doi.org/10.1007/s00429-022-02549-z

Sunaert, S., Van Hecke, P., Marchal, G., & Orban, G. A. (1999). Motion-responsive regions of the human brain. *Experimental Brain Research*, 127, 355–370. https://doi.org/10.1007/s002210050804

Tootell, R. B., Mendola, J. D., Hadjikhani, N. K., Ledden, P. J., Liu, A. K., Reppas, J. B., & Dale, A. M. (1997). Functional analysis of V3A and related areas in human visual cortex. *The Journal of Neuroscience*, 17(18), 7060–7078. https://doi.org/10.1523/JNEUROSCI.17-18-07060.1997

Tootell, R. B., Reppas, J. B., Kwong, K. K., Malach, R., Born, R. T., Brady, T. J., Rosen, B. R., & Belliveau, J. W. (1995). Functional analysis of human MT and related visual cortical areas using magnetic resonance imaging. *The Journal of Neuroscience*, 15, 3215–3230.

Tosoni, A., Pitzalis, S., Committeri, G., Fattori, P., Galletti, C., & Galati, G. (2015). Resting-state connectivity and functional specialization in human medial parieto-occipital cortex. *Brain Structure & Function*, 220, 3307–3321.

Tustison, N. J., Avants, B. B., Cook, P. A., Zheng, Y., Egan, A., Yushkevich, P. A., & Gee, J. C. (2010). N4ITK: Improved N3 bias correction. *IEEE Transactions on Medical Imaging*, 29(6), 1310–1320. https://doi.org/10.1109/TMI.2010.2046908

von Pföstl, V., Stenbacka, L., Vanni, S., Parkkonen, L., Galletti, C., & Fattori, P. (2009). Motion sensitivity of human V6: A magnetoenceph-alography study. *NeuroImage*, 45(4), 1253–1263. https://doi.org/10.1016/j.neuroimage.2008.12.058

Wada, A., Sakano, Y., & Ando, H. (2016). Differential responses to a visual self-motion signal in human medial cortical regions revealed by wide-view stimulation. *Frontiers in Psychology*, 7, 1–17. https://doi.org/10.3389/fpsyg.2016.00309

Wall, M. B., & Smith, A. T. (2008). The representation of egomotion in the human brain. *Current Biology*, 18(3), 191–194. https://doi.org/10.1016/j.cub.2007.12.053

Walther, A., Nili, H., Ejaz, N., Alink, A., Kriegeskorte, N., & Diedrichsen, J. (2016). Reliability of dissimilarity measures for multi-voxel pattern analysis. *NeuroImage*, 137, 188–200. https://doi.org/10.1016/j.neuroimage.2015.12.012

Warren, P. A., & Rushton, S. K. (2009). Optic flow processing for the assessment of object movement during ego movement. *Current Biology*, 19(18), 1555–1560. https://doi.org/10.1016/j.cub.2009.07.057

Wiest, G., Zimprich, F., Prayer, D., Czech, T., Serles, W., & Baumgartner, C. (2004). Vestibular processing in human paramedian precuneus as shown by electrical cortical stimulation. *Neurology*, 62, 473–475.

Zhang, T., & Britten, K. H. (2004). Clustering of selectivity for optic flow in the ventral intraparietal area. *Neuroreport*, 15(12), 1941–1945.

Zhang, Y., Brady, M., & Smith, S. (2001). Segmentation of brain MR images through a hidden Markov random Field model and the expectation-maximization algorithm. *IEEE Transactions on Medical Imaging*, 20(1), 45–57. https://doi.org/10.1109/42.906424

SUPPORTING INFORMATION

Additional supporting information can be found online in the Supporting Information section at the end of this article.